PNL-7326
UC-313

Inert Electrodes Program

Characterization of the Reaction Layer or Film on PNL Inert Anodes: Progress Report for April-December 1989

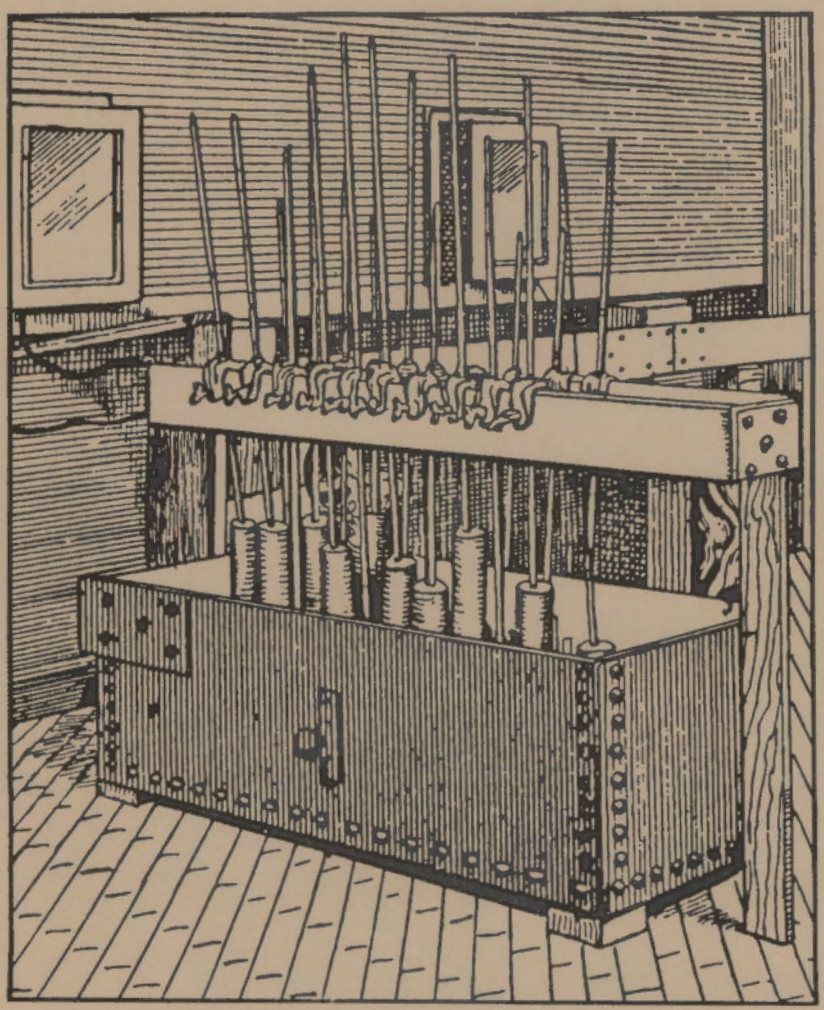

May 1990

Prepared for the U.S. Department of Energy
under Contract DE-AC06-76RLO 1830

Pacific Northwest Laboratory
Operated for the U.S. Department of Energy
by Battelle Memorial Institute

Battelle

PNL-7326

On the cover:

Aluminum reduction pots at the Pittsburgh Reduction Company's (Alcoa's) plant in 1889. Adapted from a photograph, courtesy of Alcoa.

PACIFIC NORTHWEST LABORATORY
operated by
BATTELLE MEMORIAL INSTITUTE
for the
UNITED STATES DEPARTMENT OF ENERGY
under Contract DE-AC06-76RLO 1830

Printed in the United States of America

Available to DOE and DOE contractors from the
Office of Scientific and Technical Information, P.O. Box 62, Oak Ridge, TN 37831;
prices available from (615) 576-8401. FTS 626-8401.

Available to the public from the National Technical Information Service,
U.S. Department of Commerce, 5285 Port Royal Rd., Springfield, VA 22161.

NTIS Price Codes, Microfiche A01

Printed Copy

Price Code	Page Range	Price Code	Page Range
A02	1- 10	A15	326-350
A03	11- 50	A16	351-375
A04	51- 75	A17	376-400
A05	76-100	A18	401-425
A06	101-125	A19	426-450
A07	126-150	A20	451-475
A08	151-175	A21	476-500
A09	176-200	A22	501-525
A10	201-225	A23	526-550
A11	226-250	A24	551-575
A12	251-275	A25	576-600
A13	276-300	A99	601-Up
A14	301-325		

PNL-7326
UC-313

Inert Electrodes Program

CHARACTERIZATION OF THE REACTION LAYER OR FILM ON PNL INERT ANODES:

PROGRESS REPORT FOR APRIL - DECEMBER 1989

C. F. Windisch, Jr.
N. D. Stice

May 1990

Prepared for
the U.S. Department of Energy
under Contract DE-AC06-76RLO 1830

Pacific Northwest Laboratory
Richland, Washington 99352

SUMMARY

This progress report addresses activities conducted at Pacific Northwest Laboratory (PNL) between April 1989 and December 1989 to characterize the reaction layer or film previously proposed by PNL to form on cermet anodes during the electrolytic production of aluminum in Hall-Heroult cells. Formation of this resistive film was thought to protect the cermet anode from corrosion reactions that would otherwise occur in the molten cryolite electrolyte.

The results of potential-step studies, electrochemical impedance spectroscopy, and post-mortem microscopic analysis of polarized anodes suggest that the processes of corrosion of the metallic phase of the anode and the production of oxygen gas are separable and exhibit very different kinetic behavior. The corrosion reactions occur predominantly at low anode potentials, appear to show diffusion control, and may be related to the porosity of the anode. The oxygen production reaction is the predominant reaction above 2.2 V, exhibits activation control, occurs primarily on the surface of the anode, and is accompanied by an increase in surface roughness at higher current densities.

Evidence presented in this report indicates that the production of oxygen shuts down the corrosion reactions, possibly through a pore-blocking mechanism. In addition, roughness effects may help explain some of the impedance relationships previously observed by PNL for these anodes. Although the present results do not rule out the formation of a protective layer or film, they strongly indicate mechanisms other than the formation of a macroscopic protective film for the apparent attenuation of corrosion reactions at typical operating current densities.

ACKNOWLEDGMENTS

The authors acknowledge the assistance of the staff at Pacific Northwest Laboratory (PNL), in particular the managerial guidance provided by L. G. Morgan, the technical contributions of O. H. Koski and D. M. Strachan, the microscopy work done by N. T. Saenz, and the secretarial support by D. L. Schneider. We are also grateful for the programmatic assistance provided by M. J. McMonigle, Office of Industrial Programs, U.S. Department of Energy (DOE), Washington, DC, and D. R. Segna, Richland Operations Office, DOE; and the programmatic support provided by the Office of Industrial Programs, DOE.

CONTENTS

FIGURES

TABLES

1.0 INTRODUCTION

Experimental studies conducted at Pacific Northwest Laboratory (PNL)[a] in FY 1988 and early FY 1989 indicated that the cermet inert anodes being evaluated by PNL exhibit a characteristic impedance during the electrolytic production of aluminum in bench-scale Hall-Heroult cells. This impedance was found to have the following characteristics (Strachan et al. 1988):

- It was largely resistive in nature.
- It varied as a function of current density, giving a minimum at about 0.5 A/cm^2.
- It appeared to depend on alumina concentration in the electrolyte. In general, the impedance seemed to increase with increasing alumina concentration.
- It exhibited a time dependence. Different anodes gave different impedances at different times after polarization.
- At high current densities (> 1 A/cm^2), discontinuous changes in the impedance occurred, causing "spikes" in the current or voltage data.

Based on these characteristics, PNL originally proposed that a resistive reaction layer or film (hereafter called "film") formed on inert anodes during electrolysis. It was argued that the formation of this film was necessary to protect the inert anode from corrosion reactions that would otherwise occur in the molten cryolite electrolyte. It was also proposed that an anode current density of 0.5 A/cm^2 formed a film with optimum passivating-like characteristics. At lower current densities, the film was proposed to be incompletely formed, resulting in corrosion of the cermet's metallic phase. At higher current densities, it was proposed that the film would become too thick and its resistance would become too high to sustain the current density. Consequently, the film would rupture, resulting in sudden and severe corrosion of the electrode's metal phase. The rupturing events in the film were indicated by sudden drops in impedance and appeared as "spikes" in the voltage data for a cell under galvanostatic (constant current) control.

(a) PNL is operated for the U.S. Department of Energy by Battelle Memorial Institute under Contract DE-AC 06-76RL0 1830.

It was also proposed that the quality of the film depended on the alumina concentration in the electrolyte. Higher alumina concentrations seemed to favor a more resistive, presumably thicker, film. Consequently, film rupturing behavior was considered to be more likely at high alumina concentrations (close to saturation) when current densities were above 0.5 A/cm^2. Problems with reproducibility of the experimental results were encountered, however, when attempts were made to relate anode impedance explicity to alumina concentration. It was then concluded that the film impedance was dynamic, changing with time and with small fluctuations in cell conditions.

Attempts to identify the composition of the film have been largely unsuccessful (Strachan et al. 1988). Post-mortem analyses of the anode surface region have shown the presence of alumina. However, it is uncertain whether the alumina was part of a film or whether it simply precipitated from the electrolyte adhering to the anode surface during cool-down.

During the latter part of FY 1989, experiments were performed to identify the composition of the film and to determine its characteristics more precisely, particularly those that have an impact on electrolysis efficiency. This progress report presents the results of these studies.

2.0 APPROACH TO FILM CHARACTERIZATION

Three principal techniques were used during this report period to characterize the film on the cermet inert anodes being evaluated at PNL: potential-step tests, electrochemical impedance spectroscopy (EIS), and post-mortem microscopic examination of polarized anodes.

2.1 POTENTIAL-STEP TESTS

Studying the time-dependent response of the anode to a change in cell conditions was selected since the properties of the film were proposed to be dynamic (changing with time). The approach taken in these tests was to monitor the response of current with respect to time after a sudden, controlled step in anode potential. By comparing the observed current response to that expected for different types of rate control (e.g. diffusion or charge-transfer), it was hoped that some of the mechanistic details of the reactions at the anode surface could be determined.

This report covers potential-step tests on PNL inert anodes in molten cryolite. Anode potentials range from below the decomposition potential for alumina to potentials giving current densities of about 1 A/cm^2. Molten cryolite baths containing alumina at 100%, 75%, and 50% of saturation at 983°C were studied.

2.2 ELECTROCHEMICAL IMPEDANCE SPECTROSCOPY (EIS)

In these experiments, a small ac voltage signal of varying frequency was added to the controlling voltage of a cell operating potentiostatically. The resultant ac current response was measured for each frequency and used to calculate the complex impedance of the anode, also as a function of frequency. Experiments were performed for cells at various controlling anode voltages. Plots of the real versus the imaginary portions of the complex impedance over the entire frequency spectrum contain signatures that may provide mechanistic information regarding the reactions occurring at the various potentials at the anode surface. Such plots are also called Nyquist plots.

This report discusses the results of PNL's EIS studies on cermet inert anodes in alumina-saturated molten cryolite at 983°C over a range of anode potentials.

2.3 POST-MORTEM MICROSCOPIC EXAMINATION OF POLARIZED ANODES

Optical microscopy, scanning electron microscopy (SEM), transmission electron microscopy (TEM), x-ray diffraction, and electron diffraction analysis were to be performed as needed on cermet inert anodes that had been polarized to specific potentials and current densities in molten cryolite baths of precise composition for a set period of time. It was hoped that a combination of the analytical techniques would succeed in identifying the composition of the film and determining how it depended on cell conditions, especially anode potential and alumina concentration.

Results of these studies are not yet complete. This progress report covers the results of optical microscopy on the cermet inert anodes polarized at various potentials and alumina concentrations studied by PNL.

3.0 EXPERIMENTAL PROCEDURE

Experiments were performed using the bench-scale experimental setup shown in Figure 3.1. The electrochemical cell used a three electrode arrangement. The cermet inert anode was fabricated at PNL (from $NiO/NiFe_2O_4$ oxide powder and copper metal powder to contain 17% copper by weight) according to procedures discussed in previous reports (Strachan et al. 1988). The anode was formed into the shape of a small cylinder with a cross-section of about 1 cm^2. A boron nitride (BN) sheath was used to protect the walls of the anode, allowing only one of its circular faces to be exposed to the electrolyte. This face was sanded to ensure that the anode surface in contact with the electrolyte had a similar morphology for all of the anodes used in these studies. The connector bar was a nickel rod that had been brazed to the anode during the fabrication procedure as discussed in previous reports (Strachan et al. 1988). The cathode, or counter electrode, was a graphite crucible that also served as the cell container. The crucible was large enough to hold about 1 kg of electrolyte. No aluminum metal seed was used in these tests. The reference electrode was the Al/Al_2O_3 type, fabricated according to a recently published design (Burgman, Leistra, and Sides 1986).

The electrolyte was prepared by mixing appropriate amounts of reagent grade materials to give a bath ratio equal to 1.15, 5.5% (by weight) CaF_2, 1.0% MgF_2, and alumina at the desired concentration. Studies were performed with alumina concentrations of 50%, 75%, and 100% of saturation. (Alumina concentrations in this report are given as a percent of saturation, which for these test conditions is approximately 8.0% by weight.) A temperature controller/furnace/ thermocouple arrangement was used to melt the raw materials to form a "bath" and control its temperature at 983°C. Bath ratio and temperature were effectively constant throughout these short-term tests.

The anode potential was measured and controlled using a Solartron[(a)] 1286 Electrochemical Interface. Voltage and current outputs were monitored in the potential-step tests using a strip chart recorder. For the EIS studies, a

---

(a) Solarton is a tradename of Solarton Instruments, Farmborough, Hampshire, England.

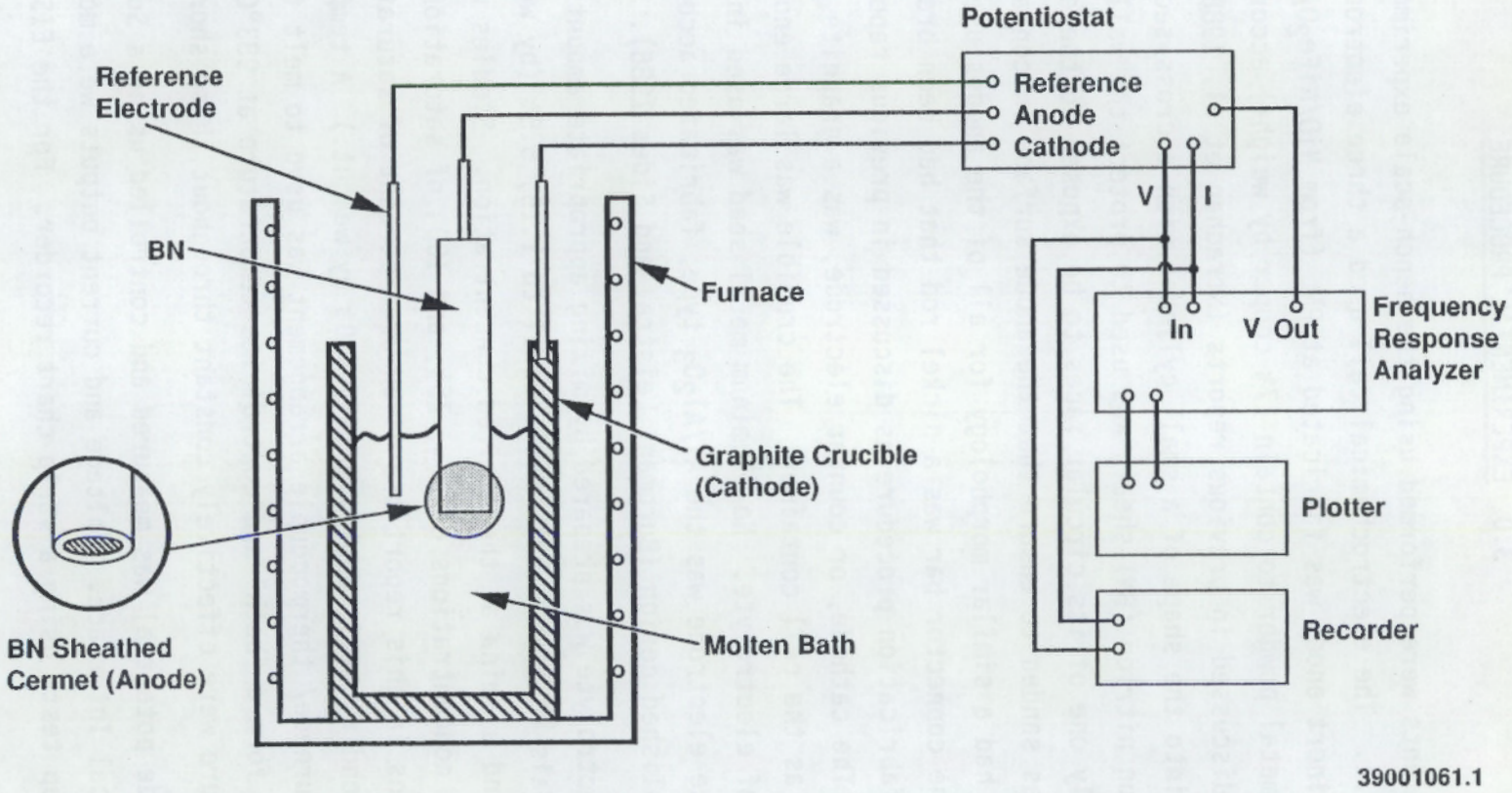

FIGURE 3.1. Apparatus for PNL Bench-Scale Laboratory Tests.

Solartron 1250 Frequency Response Analyzer was used to apply a +/- 10 mV potential to the controlling voltage, measure the current, and calculate the complex impedance. The frequency range of the excitation voltage was 0.1 Hz to 10 kHz using 20 steps per decade. Nyquist plots were obtained directly on a XY plotter.

A fresh anode was used in each study performed at a given potential and bath composition. Thus, the results of each test were not subject to variations resulting from previous polarization conditions. Consequently, in a given test, the results could be considered characteristic of only one anode potential and one bath composition.

In a typical test, the bath was first made uniformly molten at 983°C. To remove oxidizable bath impurities, a "preliminary inert anode" was then inserted and polarized to give a current of about 0.5 A for about 1 h. This electrode was then removed and the test anode was inserted. The bath temperature was allowed to reequilibrate, then the potential-step test was performed. A voltage step was applied using the potentiostat while the anode-to-reference electrode potential and anode current density were monitored using the strip chart recorder. The anode was subsequently maintained at this potential for about 1 h. During this time, EIS data were collected on the anode. After the 1 h period, the anode was removed from the bath while still under polarization conditions; the voltage was then turned off. The anode was allowed to cool in air and then submitted for analysis. The entire procedure was then repeated with a new anode at another potential. Bath compositions were changed by starting the test over and using a different compositional mix of raw materials.

For tests with alumina concentrations less than saturation, the reference electrode suffered some deterioration because its alumina outer sheath dissolved. As a result, the reference electrode had to be replaced periodically during these studies. Based on approximate weight loss measurements, it was estimated that a maximum end-of-test error of about 10% of saturation was introduced when the alumina was initially at 50% of saturation (and the dissolution rate of the reference electrode's alumina sheath was a maximum).

4.0 RESULTS AND DISCUSSION

The following is a discussion of the potential-step, EIS, and microscopy data obtained during this report period and the conclusions drawn from these data. The potential step results seem to follow a simple mathematical model. The mathematical model suggests a physical model that also appears to be consistent with the EIS and microscopy results. Although the details of this physical model are not fully resolved at this time, one possible mechanism is presented. The section concludes with discussions of data on alumina concentration dependency and surface roughness effects that support the proposed mechanism.

4.1 A MATHEMATICAL MODEL

As shown in Figures 4.1 through 4.11, the response of current to a potential-step was a sudden rise followed by a slower decay to a steady-state value. For most conditions, the majority of the current decay occurred during the first 10 s after the potential step was applied. This type of response occurs for many electrochemical systems but usually over a much shorter time interval. For example, the Cottrell equation, which accurately models the current-time relationship for many processes under mass transfer control, is usually appropriate in the millisecond regime (Macdonald 1977). The longer response time in this work suggests that actual changes in the structure and composition of the anode's surface layers may be occurring. Structural and chemical changes can be relatively slow, as in the case of the passivation of iron (Sato and Cohen 1964).

The points plotted in Figures 4.1 through 4.11 were taken from strip chart recordings of cell current. Since the exposed surface area was 1 cm^2, the ordinate values also correspond to anode current density.

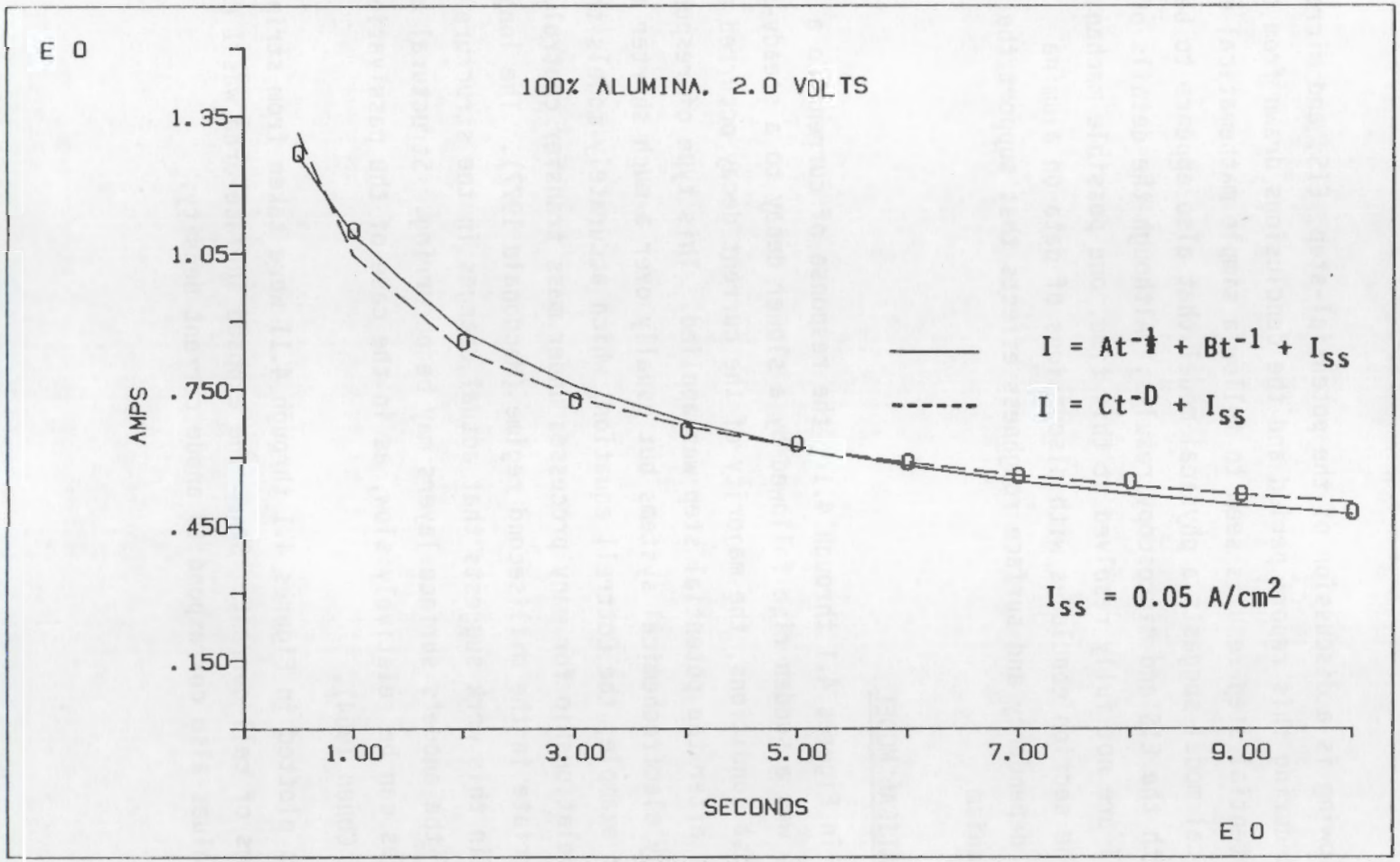

FIGURE 4.1. Potential-Step Data for 100% Alumina and 2.0 Volts.

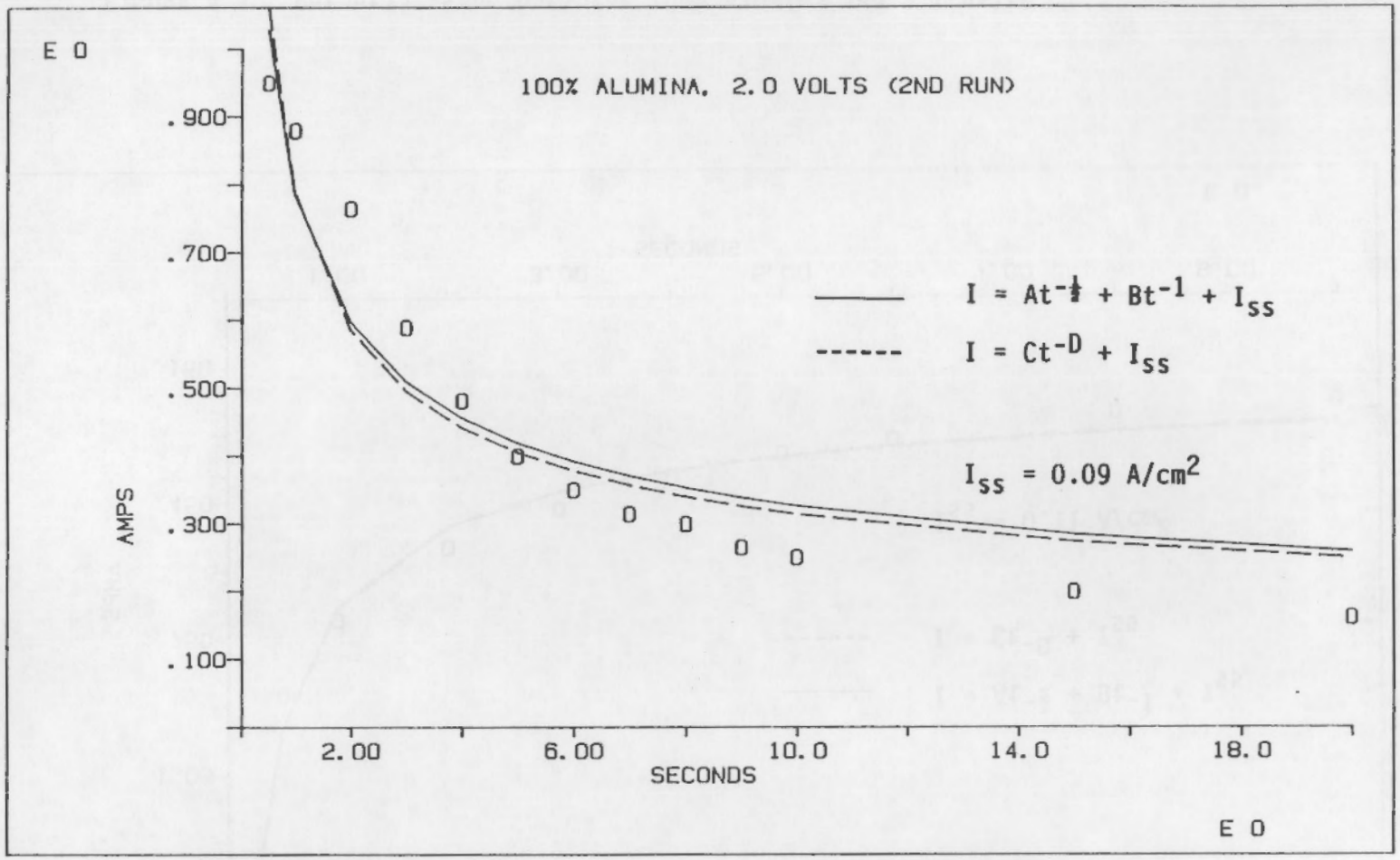

FIGURE 4.2. Potential-Step Data for 100% Alumina and 2.0 Volts. (Second Run for These Conditions.)

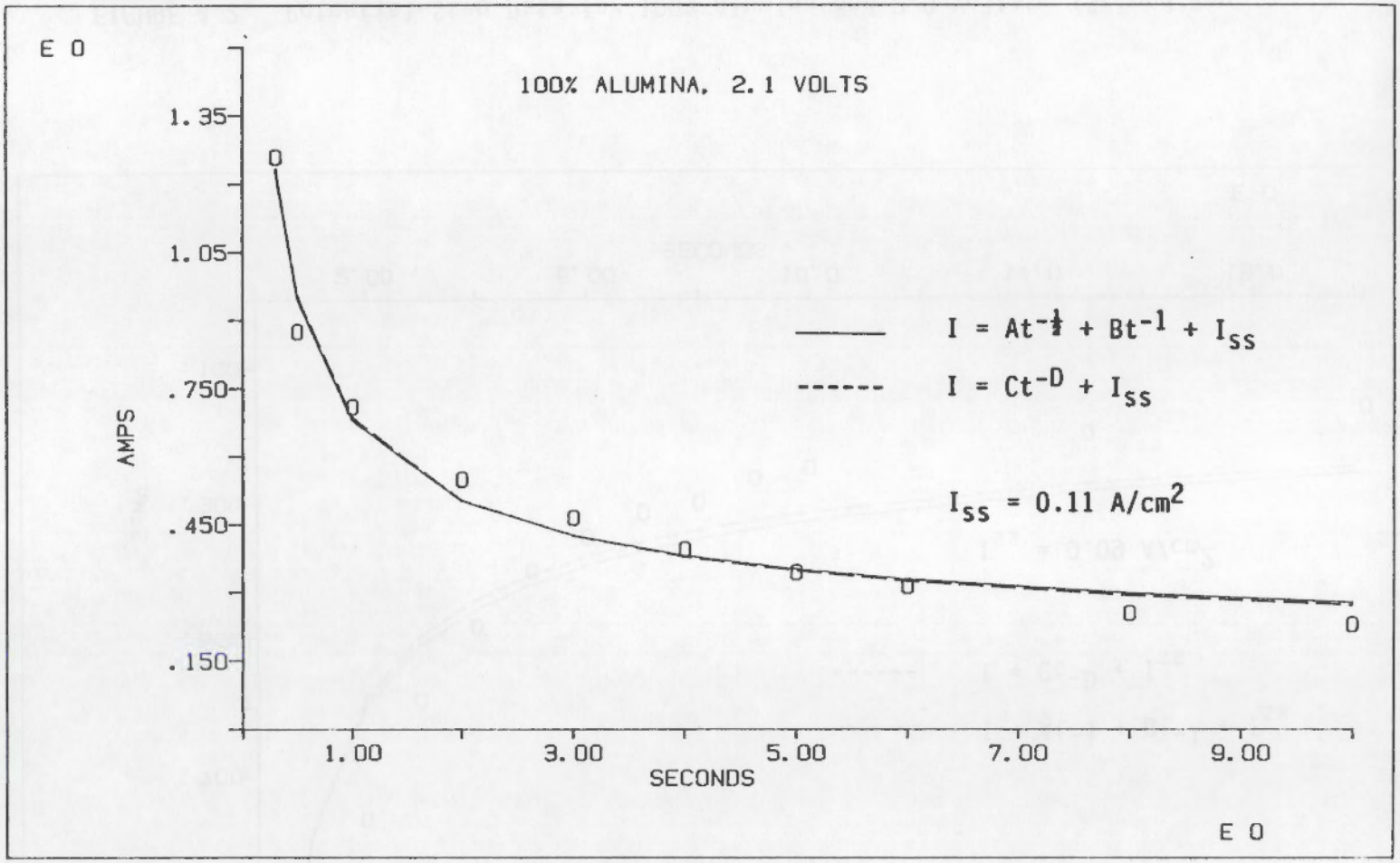

FIGURE 4.3. Potential-Step Data for 100% Alumina and 2.1 Volts.

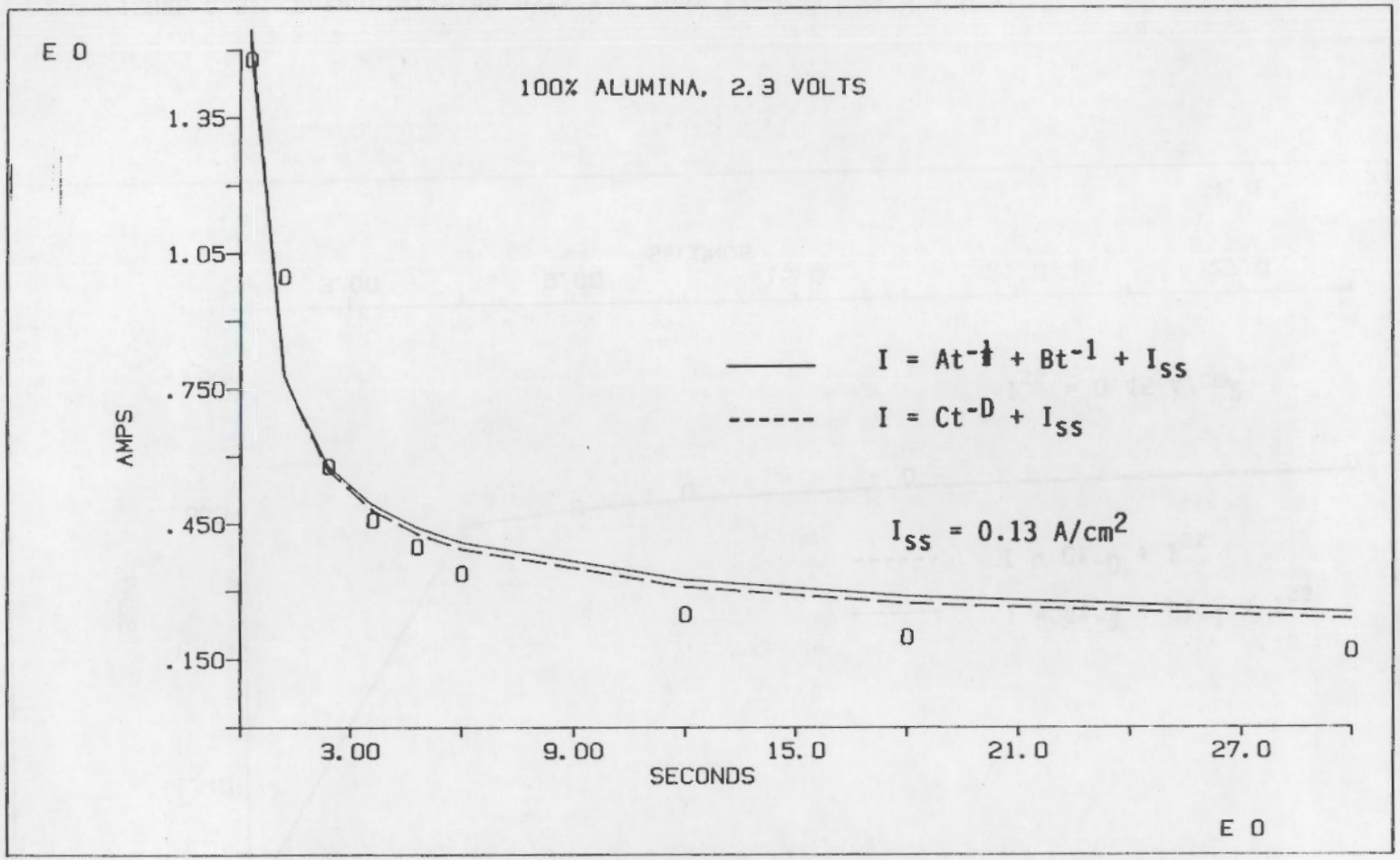

FIGURE 4.4. Potential-Step Data for 100% Alumina and 2.3 Volts.

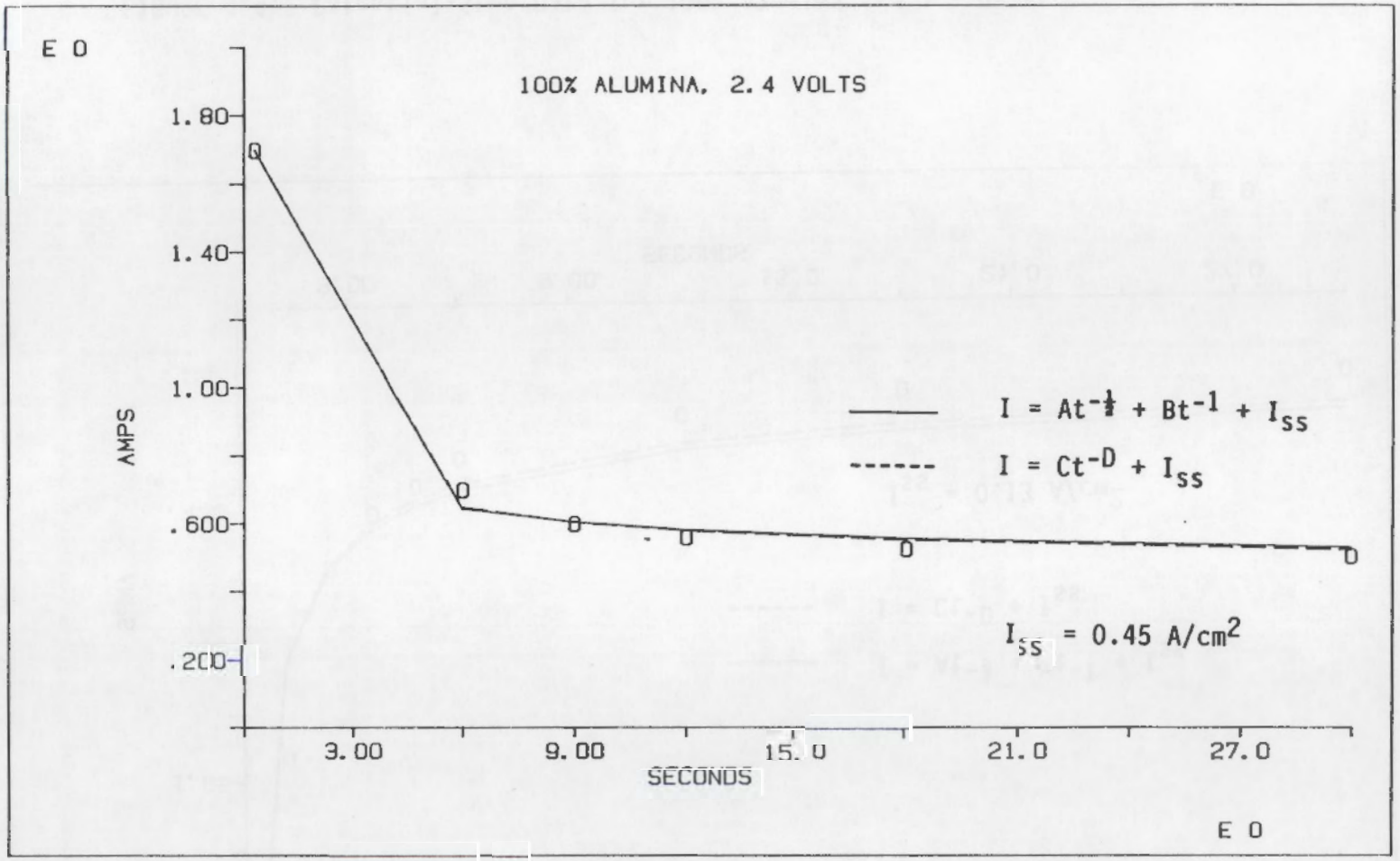

FIGURE 4.5. Potential-Step Data for 100% Alumina and 2.4 Volts.

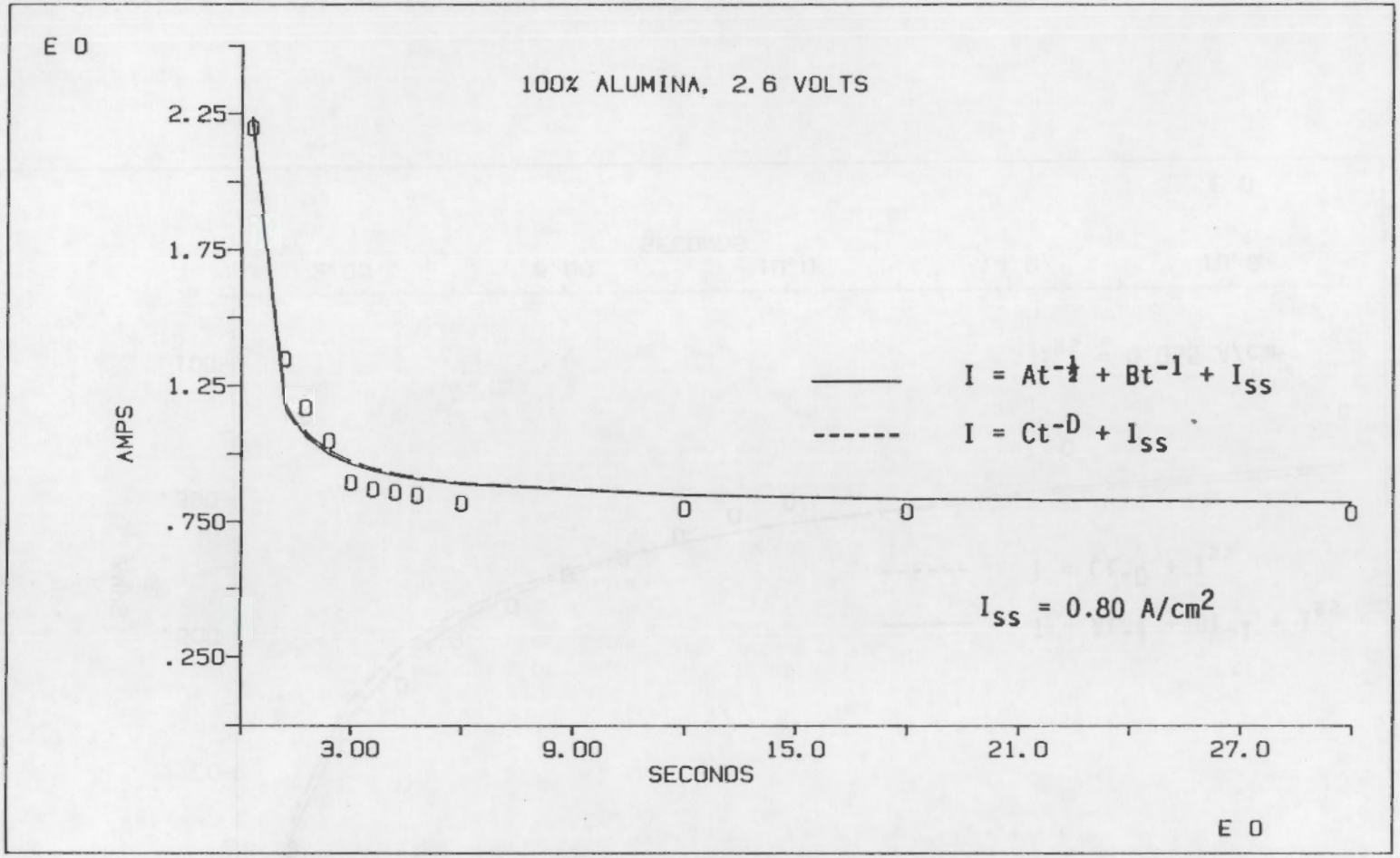

FIGURE 4.6. Potential-Step Data for 100% Alumina and 2.6 Volts.

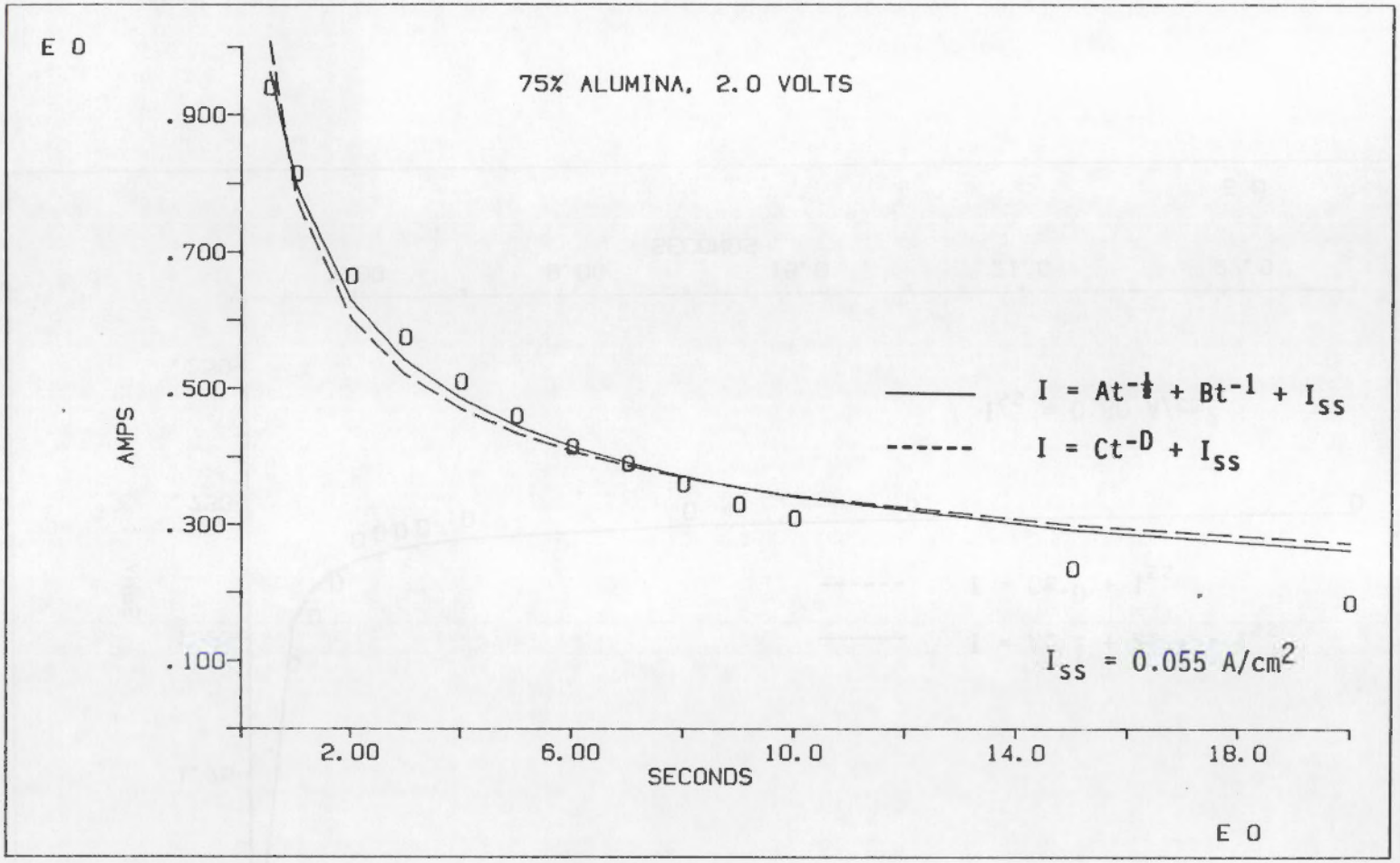

FIGURE 4.7. Potential-Step Data for 75% Alumina and 2.0 Volts.

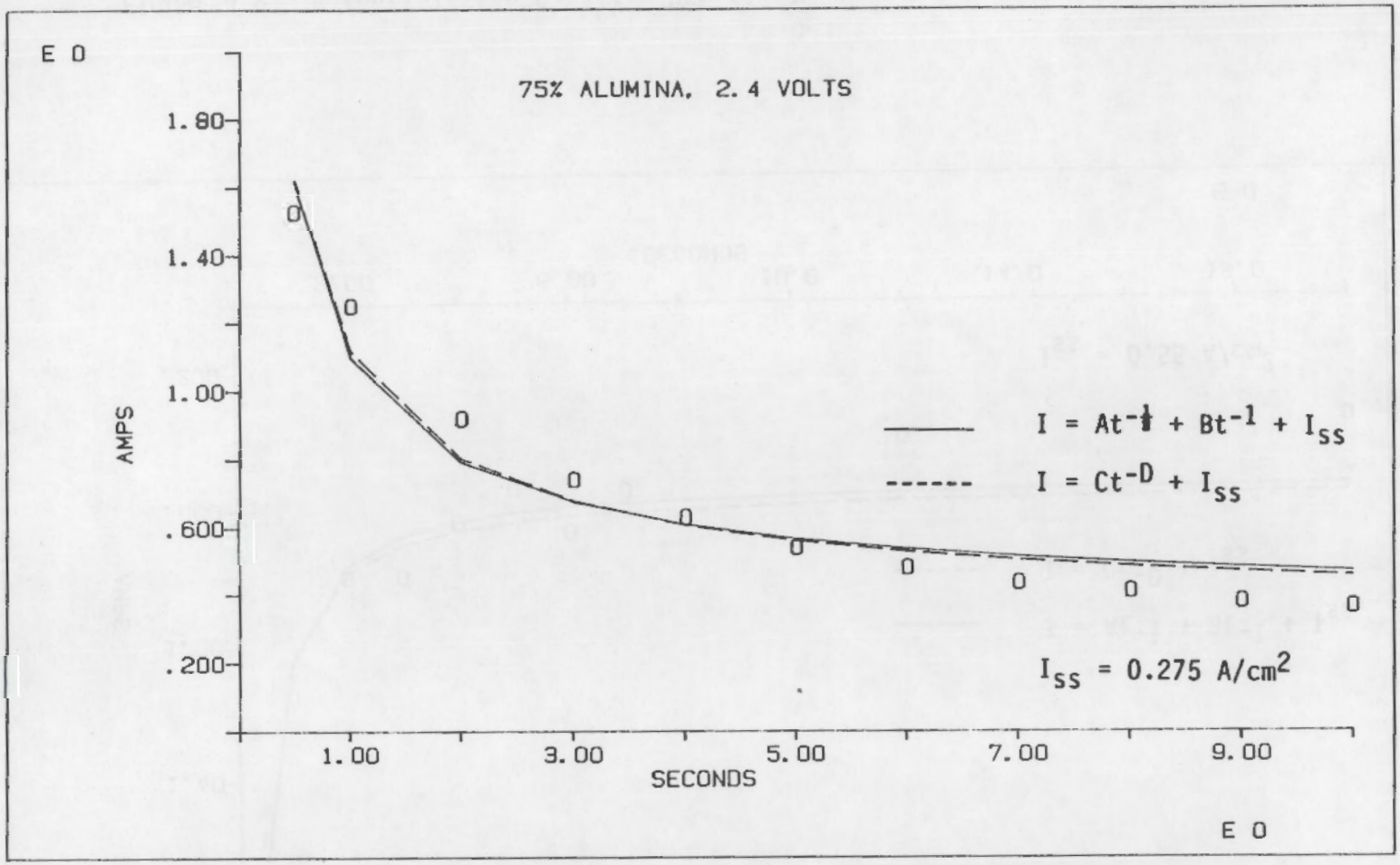

FIGURE 4.8. Potential-Step Data for 75% Alumina and 2.4 Volts.

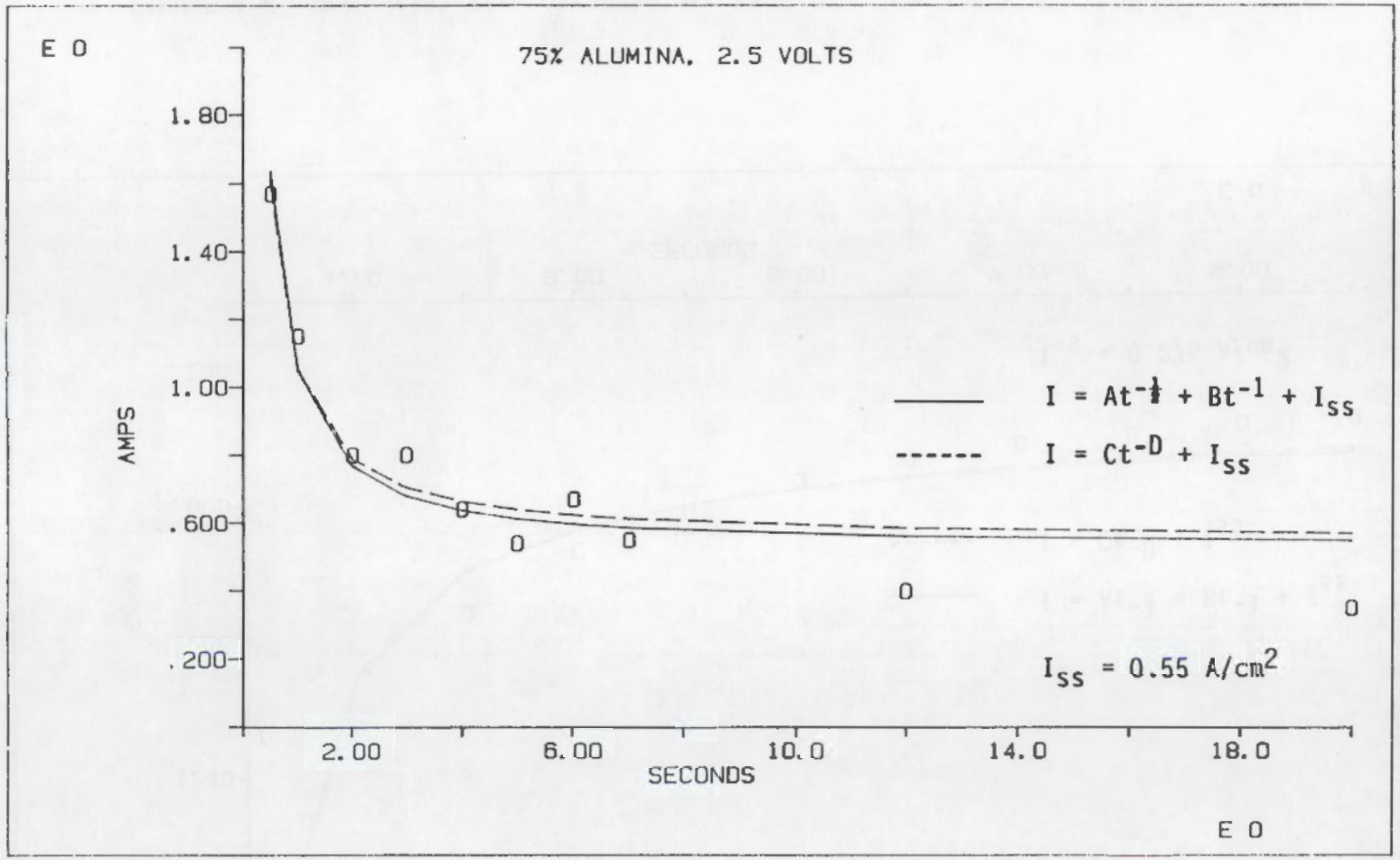

FIGURE 4.9. Potential-Step Data for 75% Alumina and 2.5 Volts.

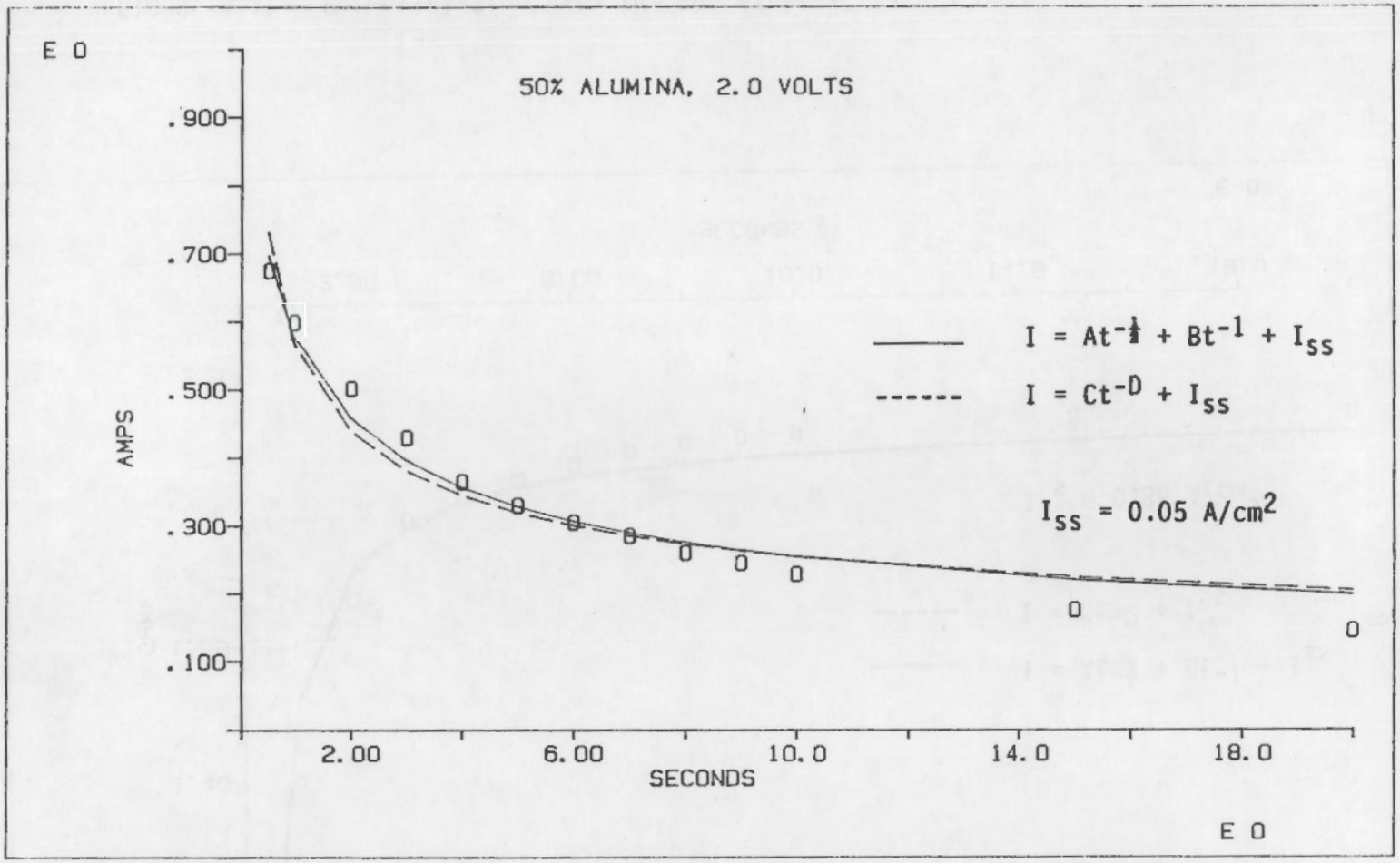

FIGURE 4.10. Potential-Step Data for 50% Alumina and 2.0 Volts.

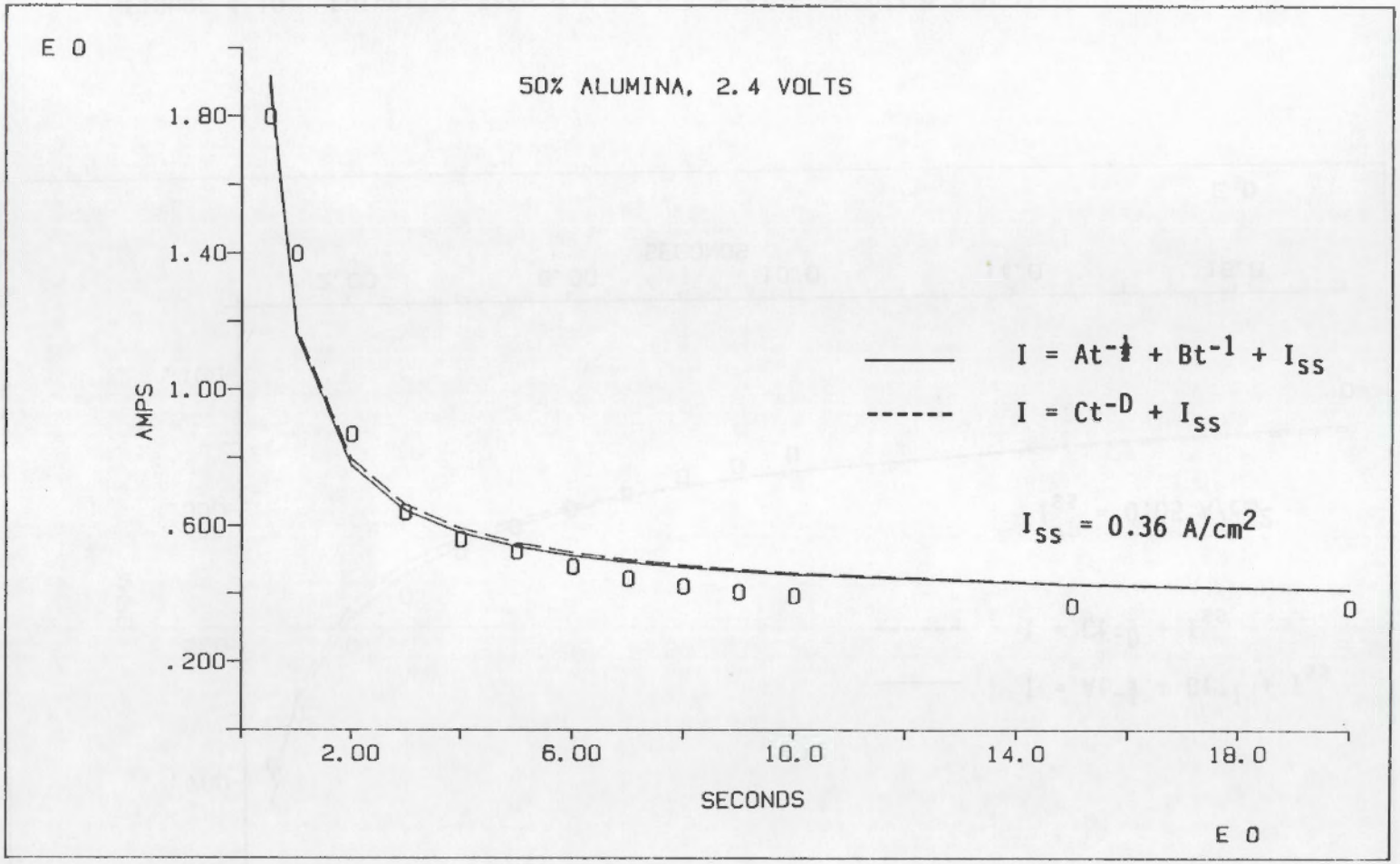

FIGURE 4.11. Potential-Step Data for 50% Alumina and 2.4 Volts.

Various mathematical models were compared with the experimental data. To limit the number of viable solutions, no more than two fitting parameters were used in any case. Two functions that gave reasonable comparison with the experimental data were the following:

$$I = At^{-\frac{1}{2}} + Bt^{-1} + I_{ss} \qquad (4.1)$$

$$I = Ct^{-D} + I_{ss} \qquad (4.2)$$

where I is the current density, t is the time from when the potential step was applied, and I_{ss} is the current density at steady-state A, B, C, and D fitting parameters. A list of the fitting parameters for the various experimental conditions tested is given in Table 4.1. The fitted curves are shown with the experimental data in Figures 4.1 through 4.11.

TABLE 4.1. Fitting Parameters

Voltage & Current Density, V/A/cm^2	%Al_2O_3	A	B	C	D	R^2(4.1)(a)	R^2(4.2)(a)
2.0/0.05	100	1.48	-0.44	1.00	0.34	0.999	0.999
2.0/0.09	100	0.77	-0.08	0.70	0.50	0.976	0.974
2.1/0.11	100	0.52	0.06	0.58	0.55	0.996	0.996
2.3/0.13	100	0.66	0.05	0.72	0.56	0.981	0.983
2.4/0.45	100	0.42	0.15	0.60	0.61	0.999	0.999
2.6/0.80	100	0.05	0.40	0.48	0.91	0.995	0.996
2.0/0.055	75	0.98	-0.24	0.72	0.40	0.996	0.992
2.4/0.275	75	0.51	0.31	0.84	0.67	0.987	0.990
2.5/0.55	75	-0.15	0.651	0.50	1.08	0.984	0.982
2.0/0.05	50	0.70	-0.17	0.99	0.40	0.995	0.990
2.4/0.36	50	0.08	0.73	0.82	0.91	0.988	0.989

(a) $R^2(1)$ and $R^2(2)$ are measures of the "goodness of fit" given by the square of the multiple correlation coefficient for the least squares fit using Equations (4.1) and (4.2), respectively.

Equation (4.1) may be interpreted as the sum of three independent contributions to current density. The steady-state current, I_{ss}, is constant and arises from the oxygen production reaction at the electrode surface[a]

$$O^{2-} \longrightarrow 1/2\ O_2 + 2e^- \qquad (4.3)$$

and/or the steady-state rates of any corrosion processes involving the metallic phase of the cermet anode such as

$$Ni \longrightarrow Ni^{2+} + 2e^- \qquad (4.4)$$

$$Cu \longrightarrow Cu^{n+} + ne^- \qquad (5.5)$$

where n is either 1 or 2.

The A-term in Equation (4.1) corresponds to a diffusion-type contribution and the B-term to a process involving the linear growth of a resistive layer. (If resistance is linear with time, current is inversely related to time). Expressed in the form of a sum, the coefficients A and B should give an indication of the relative importance of these two dynamic parts of the process.

As shown in Figure 4.12, the coefficients A and B appear to be inversely related to each other. As A increases in magnitude, B becomes smaller. In other words, the more important diffusion is in limiting the current density, the less important the linear growth term is, and visa versa. Figure 4.13 shows that, for all of the alumina concentrations examined, A is largest at low current densities and decreases almost linearly with increasing current density. B, on the other hand, is smallest at low current densities and increases almost linearly with increasing current density. The relationship of the terms A and B also appears to show a dependency on alumina concentration that will be discussed later.

(a) The oxygen-containing ionic species is given as O^{2-} for simplicity. Actually the species have been identified as $Aly_2OF_6^{2-}$ and $Al_2O_4^{2-}$ (Sterten 1980).

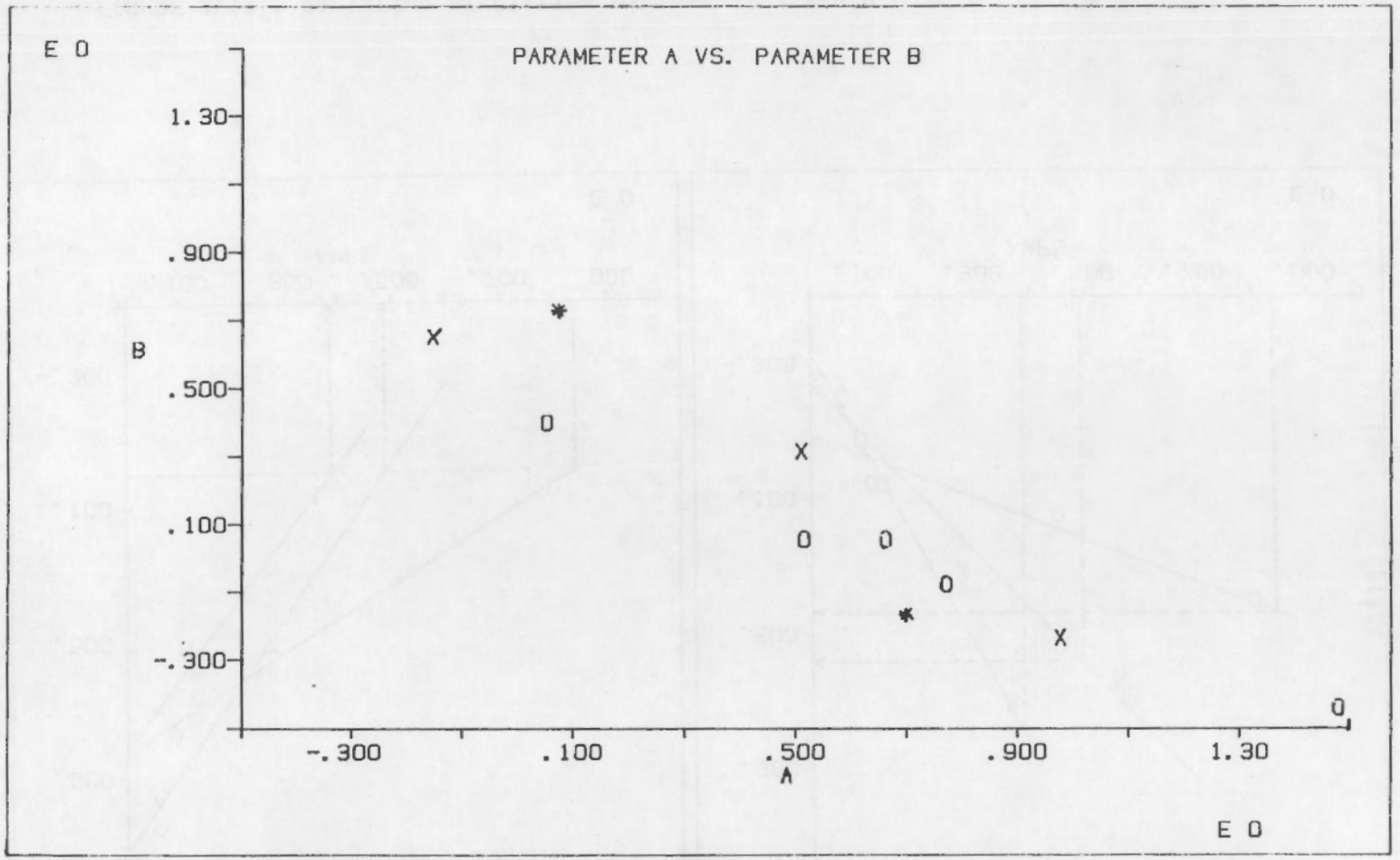

FIGURE 4.12. Plot of Fitting Parameter A Versus Fitting Parameter B for 100% (0), 75% (X) and 50% (*) Alumina.

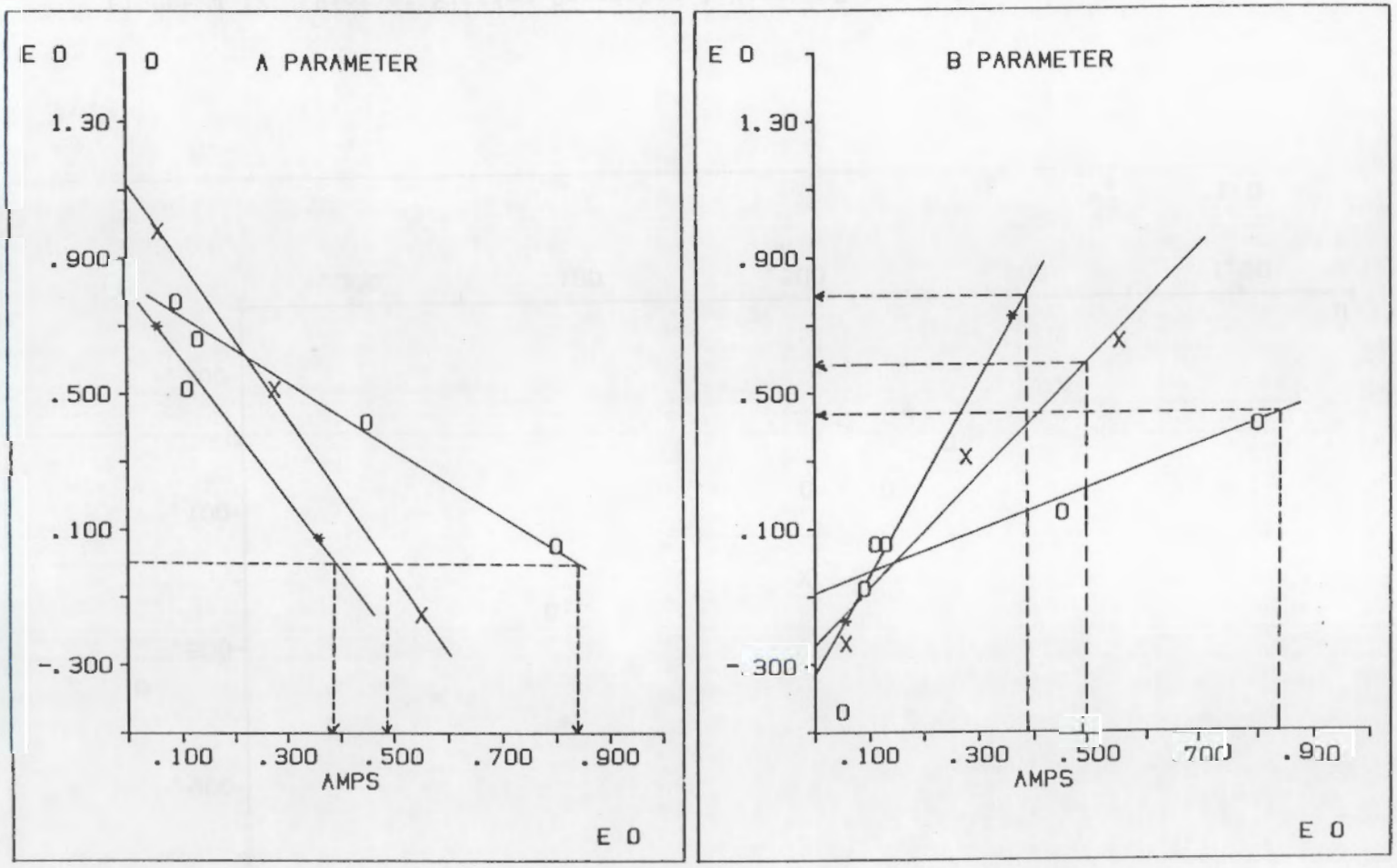

FIGURE 4.13. Variation of Fitting Parameters A and B With Current for 100% (O), 75% (X) and 50% (*) Alumina. (Dashed lines are for developing Figure 4.19. See text.)

The above results suggest that a diffusion-limited process is important at low current densities and a process involving the linear growth of a resistive layer is important at high current densities. At intermediate current densities (the exact value depends on alumina concentration), both the diffusion and linear growth terms are current limiting.

Similar conclusions are reached by considering Equation (4.2). Figure 4.14 shows how coefficients C and D vary with current density. D varies from about 0.5 at low current density to about 1.0 at high current density, again suggesting the transition from a diffusion-type process to a linear growth-type process with increasing current density. The values for C do not appear to contain much relevant information.

4.2 A PHYSICAL MODEL

A physical model can be derived from the mathematical relationship in Equation (4.1) by first recognizing that the total cell current is the sum of currents from the reactions expressed by Equations (4.3), (4.4) and (4.5). The oxygen production reaction illustrated by Equation (4.3) occurs mostly on the surface of the anode and the corrosion reactions expressed by Equations (4.4) and (5.5) occur mainly in the anode's pores (Tarcy 1986). Thus, the total current can be expressed as the following:

$$I^{p}_{corr} + I^{s}_{ox} \qquad (4.6)$$

where I^{p}_{corr} is the current from corrosion reactions in the pores and I^{s}_{ox} is the current from oxygen production occurring mainly on the anode's outer surface.

4.2.1 Low Current Density Behavior

The decomposition potential for alumina is 2.2 V versus the Al/Al_2O_3 electrode. Consequently, current produced below (or near) this potential predominantly arises from the corrosion reactions illustrated by Equations (4.4) and (4.5),[(a)] and occurring primarily in the pores of the anode.

(a) Some sub-decomposition potential production of oxygen may also contribute to this current although its role is probably minor (Tarcy 1986).

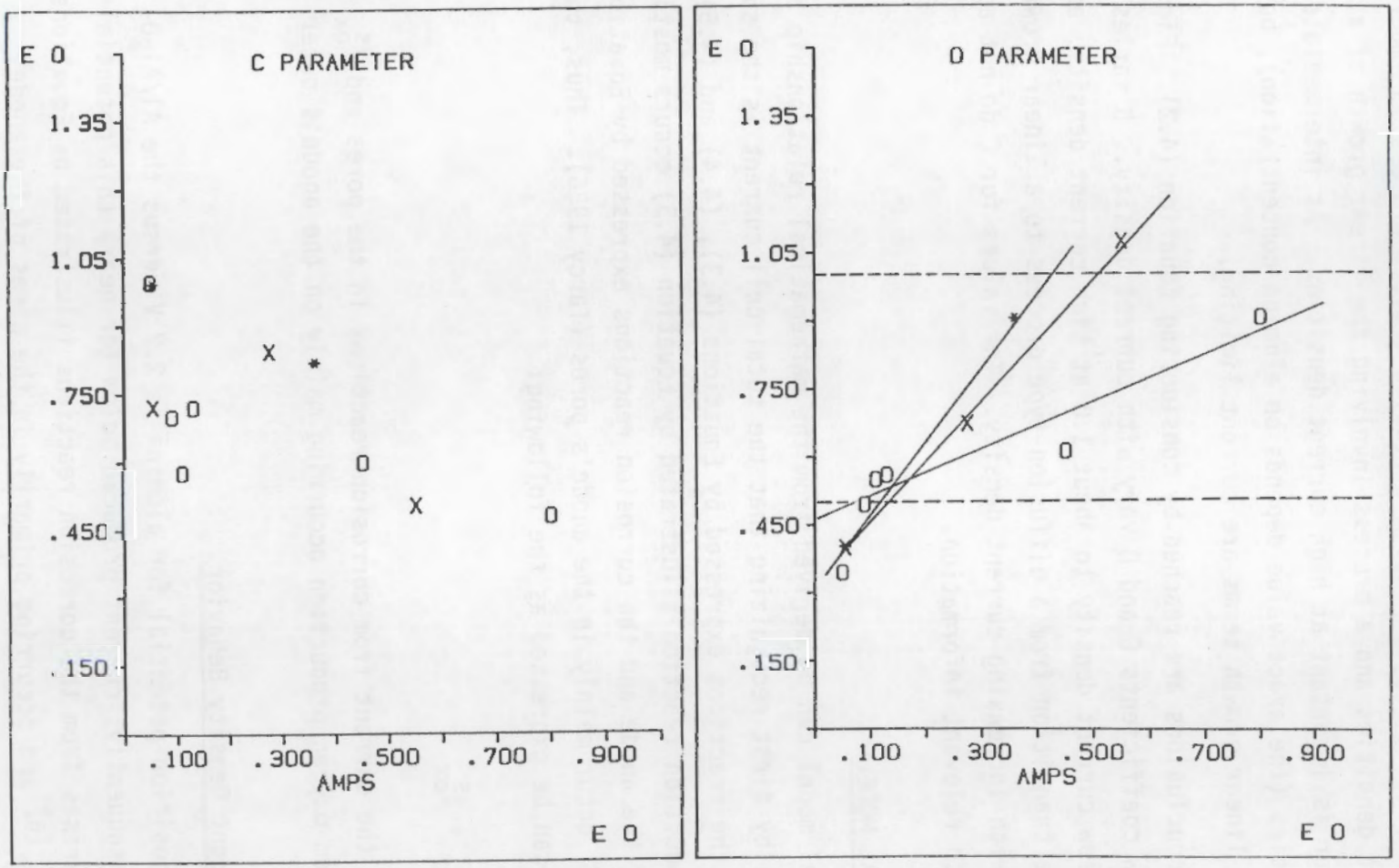

FIGURE 4.14. Variation of Fitting Parameters C and D with Current for 100% (0), 75% (X) and 50% (*) Alumina.

$$I = I^{p}_{corr} \qquad \text{(low cd)} \tag{4.7}$$

This supposition is supported by post-mortem microscopy at PNL of cermet inert anodes polarized at potentials below 2.2 V. Figure 4.15a is an optical micrograph of an unpolarized anode submerged momentarily in molten cryolite; Figure 4.15b shows an anode polarized at 2.1 V for 1 h (Figure 4.15c will be discussed later). The darker regions in the cermet portions of both micrographs are oxide phases; the very light phase is metallic. Only the bottom surface of the anode was exposed to the electrolyte. A comparison of Figures 4.15a and 4.15b shows that the surface region of the polarized anode degraded severely. The degradation was characterized by increased porosity and loss of the metallic phase. Clearly, corrosion reactions are important at relatively low anode potentials.

The potential-step data suggest that the low current density data is diffusion limited, which is also consistent with the reactions occurring in pores. Corrosion of the metal phase in similar cermet anodes was previously proposed (Tarcy 1986) to be diffusion limited and occur in pores. In addition, diffusion-controlled anodic reactions occurring on some types of carbon anodes have been explained by considering the porosity of the carbon (Thonstad 1970). As shown in Figure 4.16, EIS data for the cermet inert anode at 2.1 V in alumina-saturated molten cryolite are also consistent with a diffusion-limited reaction and with the role of porosity. The Nyquist plot (or a plot of the real part, Z', versus the imaginary part, -Z", of the complex impedance) shows a low-frequency region that is characterized by an apparently linear increase of -Z" with Z'. This is typical for a Warburg-type diffusion (Bard and Faulkner 1980). For planar electrodes the phase angle, or inverse tangent of the slope of this line, should be 45 degrees. For porous electrodes (deLevie 1967), the phase angle will be less than 45 degrees (ideally, 22.5 degrees for semi-infinite pores). The measured phase angle is 32 degrees, again consistent with the behavior of a porous electrode.

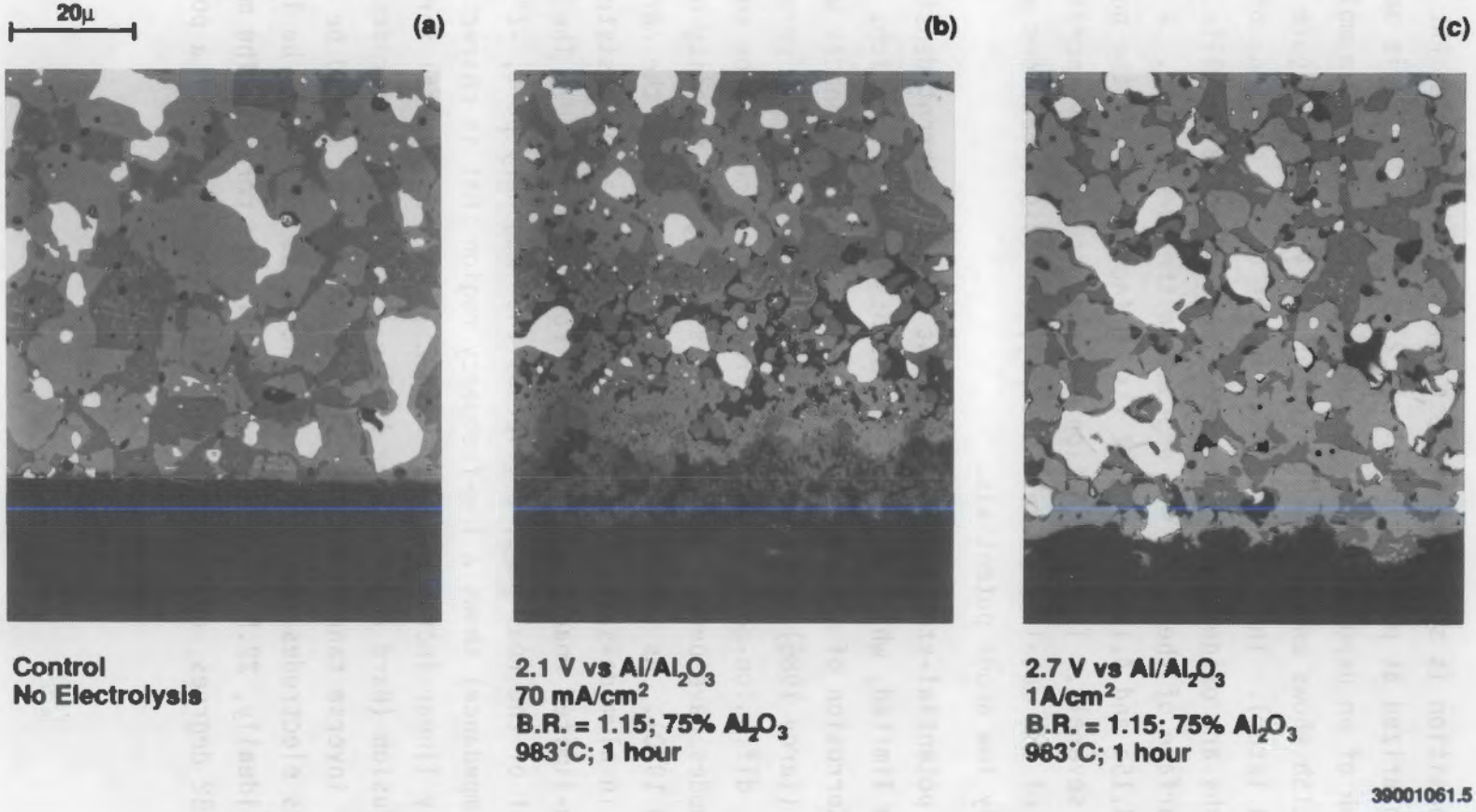

FIGURE 4.15. Optical Micrographs for PNL Cermet Inert Anodes.

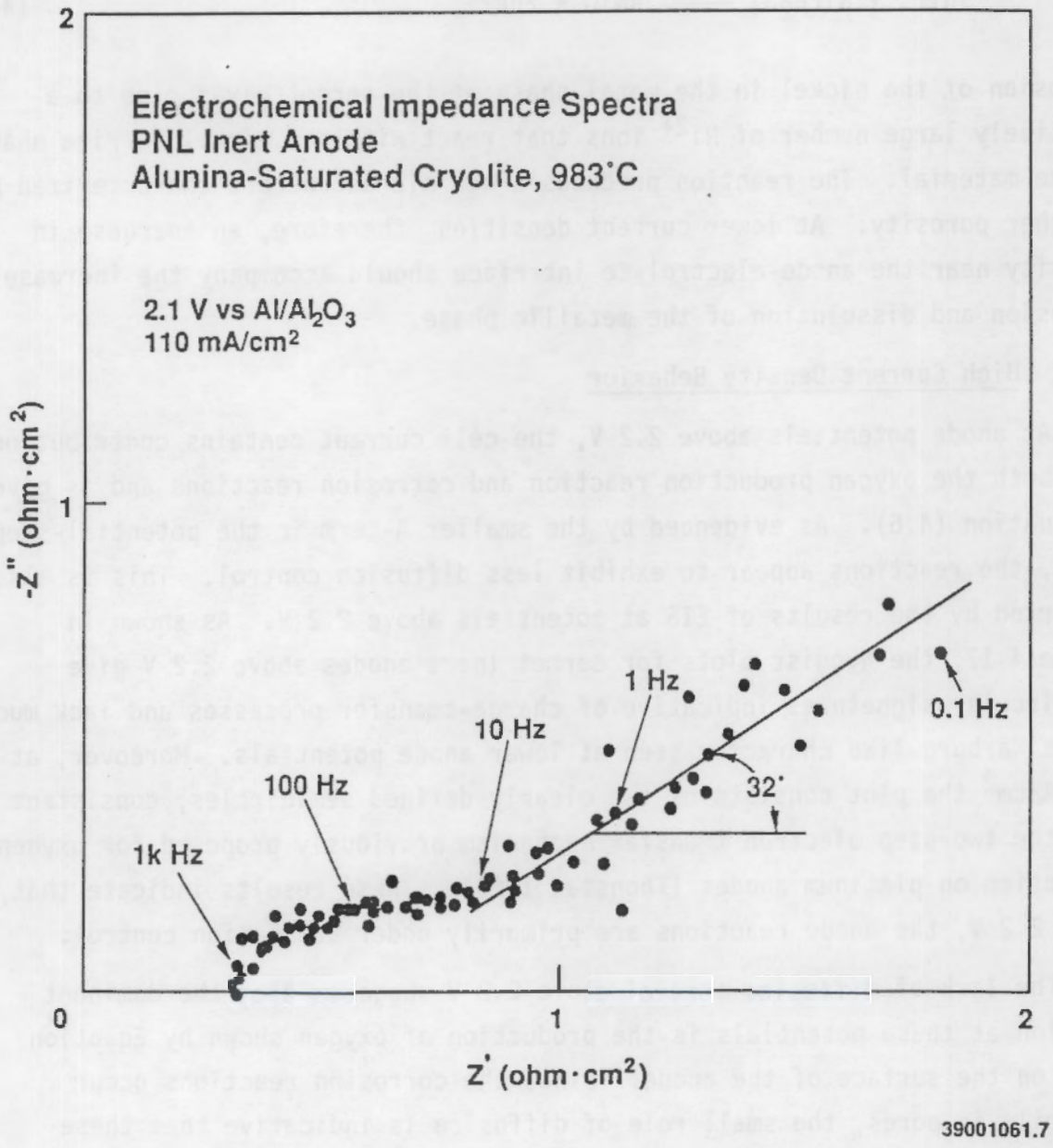

FIGURE 4.16. Electrochemical Impedance Spectra for PNL Inert Anode at 2.1 Volts.

The increased porosity observed on anodes polarized at lower current densities can be explained by the following parasitic reaction which was proposed to occur in nickel-containing cermets (Tarcy 1986):

$$3Ni^{2+} + NiFe_2O_4 \longrightarrow 4NiO + 2Fe^{3+} \qquad (4.8)$$

Corrosion of the nickel in the metal phase of the cermet gives rise to a relatively large number of Ni^{2+} ions that react with the nickel ferrite phase of the material. The reaction produces a new microstructure characterized by a higher porosity. At lower current densities, therefore, an increase in porosity near the anode-electrolyte interface should accompany the increase in corrosion and dissolution of the metallic phase.

4.2.2 High Current Density Behavior

At anode potentials above 2.2 V, the cell current contains contributions from both the oxygen production reaction and corrosion reactions and is given by Equation (4.6). As evidenced by the smaller A-term in the potential-step tests, the reactions appear to exhibit less diffusion control. This is also supported by the results of EIS at potentials above 2.2 V. As shown in Figure 4.17, the Nyquist plots for cermet inert anodes above 2.2 V give semicircular signatures indicative of charge-transfer processes and lack much of the Warburg-like character seen at lower anode potentials. Moreover, at 440 mA/cm^2 the plot consists of two clearly defined semicircles, consistent with the two-step electron transfer mechanism previously proposed for oxygen production on platinum anodes (Thonstad 1968). These results indicate that, above 2.2 V, the anode reactions are primarily under activation control.

The lack of diffusion control above 2.2 V suggests that the dominant reaction at these potentials is the production of oxygen shown by Equation (4.3) on the surface of the anode. Since the corrosion reactions occur primarily in pores, the small role of diffusion is indicative that these reactions provide little contribution to the steady-state current at potentials above 2.2 V.

$$I = I^{s}_{ox} \qquad \text{(high cd, steady-state)} \qquad (4.9)$$

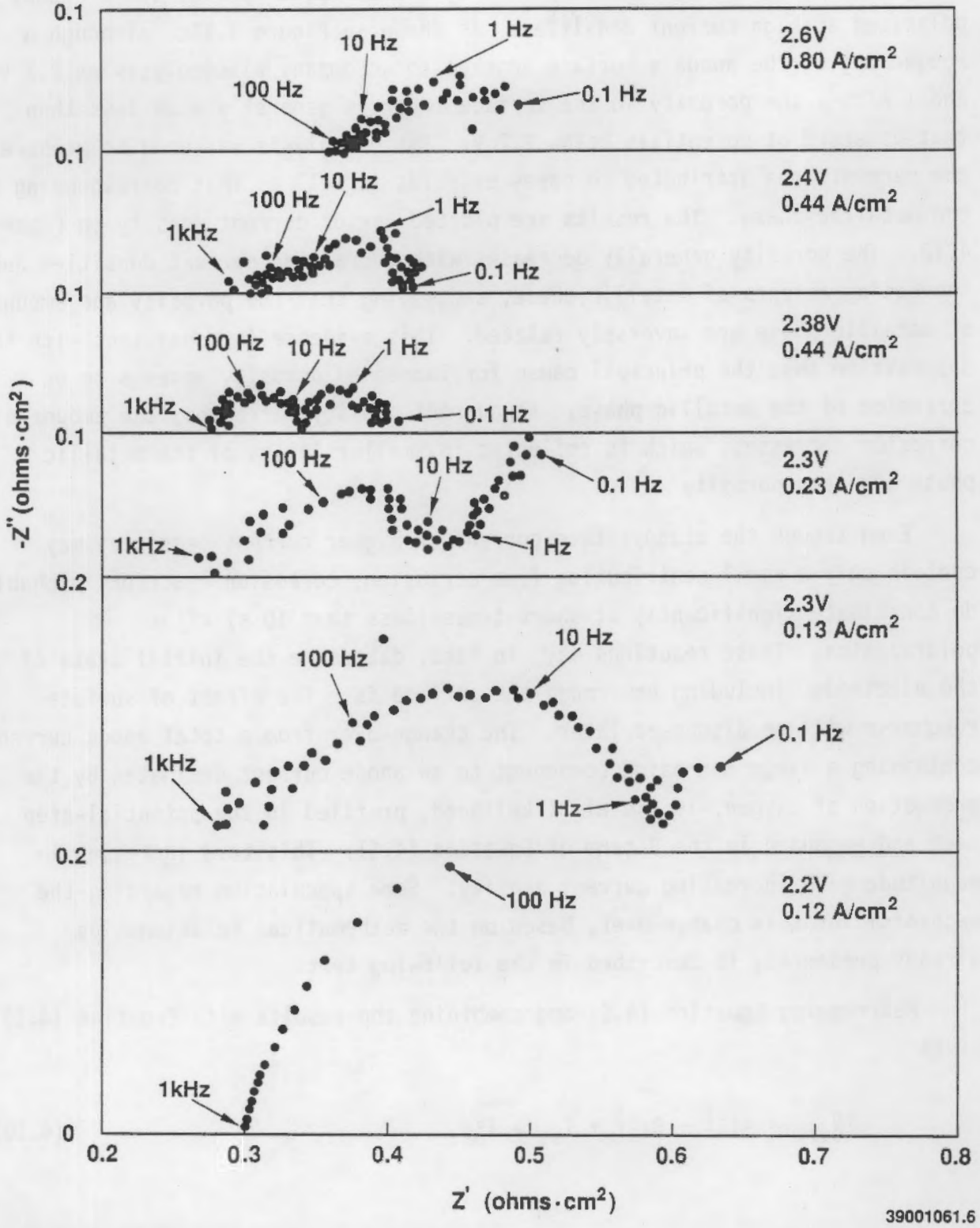

FIGURE 4.17. Electrochemical Impedance Spectra for PNL Inert Anodes at Potential Above 2.1 Volts.

This conclusion is also supported by microscopy of cermet inert anodes polarized at high current densities. As shown in Figure 4.15c, although a roughening of the anode's surface appears to accompany electrolysis at 2.7 V and 1 A/cm^2, the porosity in the surface layer is generally much less than that observed at potentials below 2.2 V. Image analysis was used to measure the percent area attributed to pores or voids as well as that corresponding to the metallic phase. The results are plotted versus current density in Figure 4.18. The porosity generally decreases with increasing current densities and increasing amounts of metallic phase, suggesting that the porosity and amount of metallic phase are inversely related. This evidence is consistent with the supposition that the principal cause for increased porosity appears to be corrosion of the metallic phase. As current density increases, the amount of corrosion decreases, which is reflected in smaller losses of the metallic phase and less porosity.

Even though the steady-state current at higher current densities may contain only a small contribution from corrosion, corrosion reactions probably do contribute significantly at short times (less than 10 s) after polarization. These reactions may, in fact, determine the initial state of the electrode, including how rough the surface is. The effect of surface roughness will be discussed later. The change-over from a total anode current containing a large corrosion component to an anode current dominated by the production of oxygen, is, in all likelihood, profiled in the potential-step data and embodied in the B-term of Equation (4.1). This term increases in magnitude with increasing current density. Some speculation regarding the mechanism for this change-over, based on the mathematical relationships already presented, is described in the following text.

Rearranging Equation (4.6) and combining the results with Equation (4.1) gives

$$I^{p}_{corr} = At^{-\frac{1}{2}} + Bt^{-1} + I_{ss} - I^{s}_{ox.} \qquad (4.10)$$

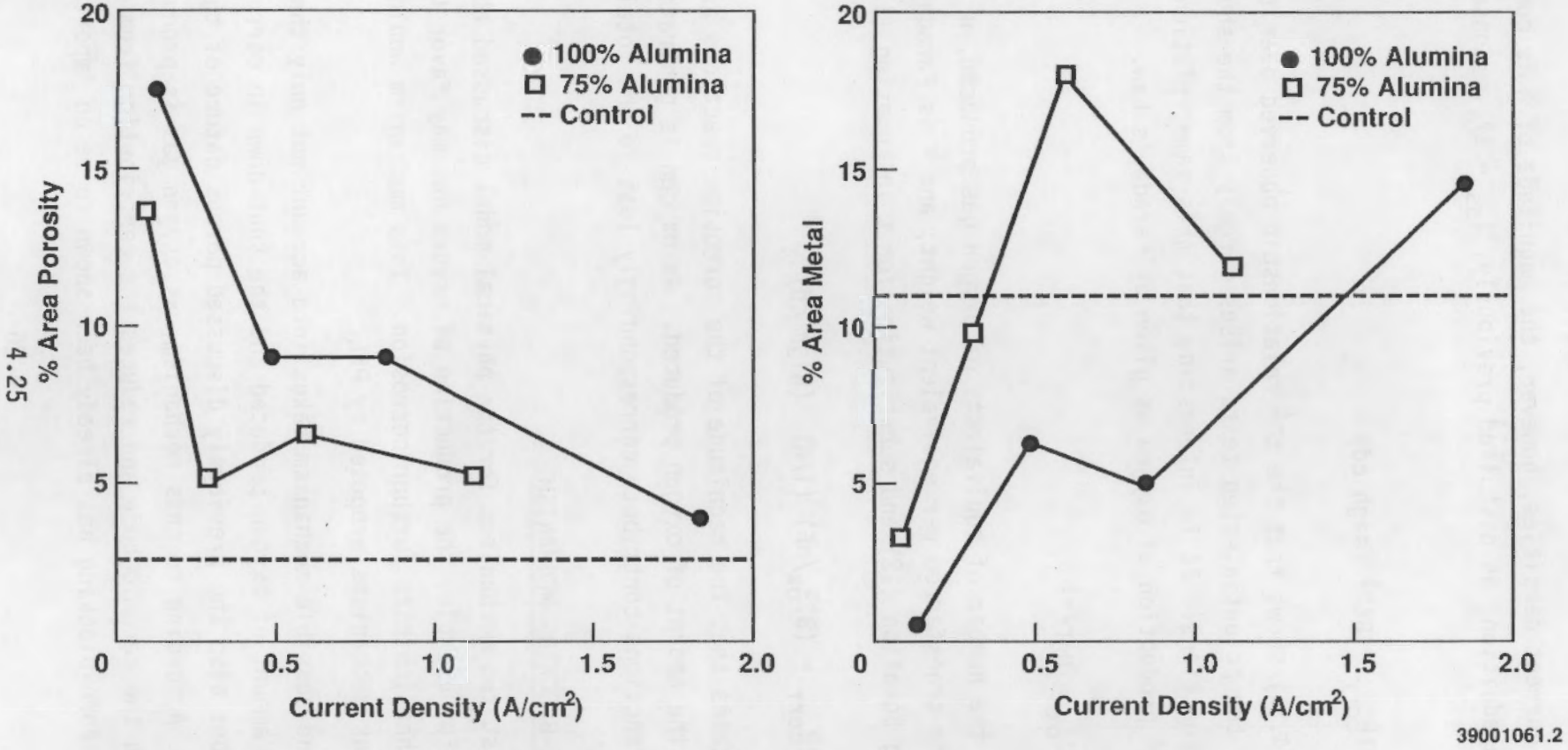

FIGURE 4.18. Porosity and Metal Phase Relationships in 0.50μ Surface Region on PNL Cermet Inert Anodes. Data are for 100% (•) and 75% (□) Alumina and for an Unpolarized Specimen (---).

At higher current densities, however, the magnitude of A is comparatively small. In addition, as discussed previously, $I_{ss} = I^{s}_{ox}$. Consequently, we can write

$$I^{p}_{corr} = Bt^{-1} \text{ (high cd)} \tag{4.11}$$

Equation (4.11) shows that the t^{-1} relationship observed over the first 10 seconds in the potential-step tests arises largely from the shut-down of the corrosion reactions. It is interesting that this same relationship describes the rate of production of oxygen as given by Faraday's Law.

$$I^{s}_{ox} = NnFt^{-1} \tag{4.12}$$

where N is the number of equivalents of oxygen gas produced, n is the number of electrons transferred per equivalent weight, and F is Faraday's constant. Rearranging Equation (12) and substituting for t in Equation (11) gives

$$I^{p}_{corr} = (BI^{s}_{ox}/nF)\ (1/N) \quad \text{(high cd)} \tag{4.13}$$

which indicates that the magnitude of the corrosion reactions are inversely related to the amount of oxygen produced. As oxygen is generated, the corrosion reactions contribute correspondingly less to the total current.

4.3 A PORE-BLOCKING MECHANISM

At least two mechanisms for the physical model discussed above are possible. For example, the production of oxygen gas may favor the formation of a film that inhibits further corrosion. This mechanism would be consistent with previous mechanisms proposed by PNL.

A second possible mechanism takes into account not only the relationship between the amount of oxygen produced and the shut-down in corrosion reactions, but also the previously discussed porous nature of the cermet electrodes. According to this mechanism, as oxygen gas is produced it plugs the pores in the ceramic body and reduces the contribution from corrosion reactions. Pore-blocking has already been shown to be an important part of

the corrosion behavior of cermets containing nickel metal (Tarcy 1986). Therefore, it should not be surprising that the phenomenon also contributes to the behavior of copper-containing cermets.

This second mechanism has a number of distinct advantages over the film-forming mechanism. Minimal diffusion effects should be observed at these current densities if most of the oxygen gas is produced on the surface of the electrode. This prediction is consistent with the potential-step and EIS data. If a film were formed as previously proposed, transport across it would give rise to some diffusional characteristics, particularly if the film is resistive as previous reported. Lack of diffusion control leaves the question of charge transport across the film unanswered. In addition, the existence of the pore-blocking mechanism eliminates the need to "find" and unequivocally identify a reaction layer or film.

4.4 THE RELATIONSHIP BETWEEN FITTING PARAMETER B AND THE CONCENTRATION OF ALUMINA

The pore-blocking theory is also consistent with the way in which the corrosion processes are influenced by alumina concentration.

The mechanism (Thonstad 1968) for the production of oxygen gas on an inert electrode (Pt) is the following:

$$O^{2-} \xrightarrow{k_1} O(ad) + 2e^- \qquad (4.14)$$

$$O^{2-} + O(ad) \xrightarrow{k_2} O_2(ad) + 2e^- \qquad (4.15)$$

$$O_2(ad) \xrightarrow{k_3} O_2(g) \qquad (4.16)$$

where the k values are the various rate constants and (ad) refers to adsorbed species. Based on this mechanism, the overall reaction rate of oxygen production at the anode surface, dX^S/dt, is[(a)]

$$dX^S/dt = k_1C' \tag{4.17}$$

where C' is the concentration of oxide ion O^{2-} in moles per cm^3 of molten electrolyte.

Using the chain rule,

$$(dR^p_{ox}/dt)(dX^p/dR^p_{ox})(dX^S/dX^p) = k_1C' \tag{4.18}$$

where (dR^p_{ox}/dt) is the rate of increase in electrical resistance resulting from oxygen infusing the pores, (dX^p/dR^p_{ox}) is the reciprocal of resistance per amount of oxygen gas in the pores (r), and (dX^S/dX^p) is the reciprocal of the fraction of the oxygen produced on the surface that finds its way into the pores (f). Rewriting the above equation,

$$dR^p_{ox}/dt = frk_1C' \tag{4.19}$$

Rearranging and integrating Equation (4.19) gives

$$R^p_{ox} = frk_1C't \tag{4.20}$$

The constant of integration is zero since the initial amount of oxygen in the pores is taken as zero along with the initial R^p_{ox}.

Using Ohm's Law, the corrosion current in the pores is therefore given by

$$I^p_{corr} = V^p/R^p_{ox} = (V^p/frk_1C')(1/t) \tag{4.21}$$

where V^p is the "pore potential."

(a) Derived by using the steady-state approximation on the adsorbed species O(ad) and O_2(ad).

Comparison of Equation (4.11) and Equation (4.21) gives

$$B = (V^P/frk_1)(1/C') \tag{4.22}$$

or

$$B = (V^P/3frk_1)(1/C) \tag{4.23}$$

where C is the concentration of alumina in moles per cm^3 of molten electrolyte.

Assuming $(V^P/3frk_1)$ is constant, as a first approximation,[(a)] and that the mechanism holds throughout the range of alumina concentrations, Equation (4.23) says that a plot of fitting parameter B for various concentrations of alumina versus 1/C is a straight line with a B-intercept equal to zero.

Fitting Parameter B was determined from Figure 4.12 for alumina concentrations equal to 100%, 75%, and 50% of saturation. The appropriate value for B was selected by first determining the current density when A was equal to zero. At this current density the contribution from the A-term was considered acceptably small (consistent with the use of Equation (4.11) in the above derivation). The value of B for this current density was subsequently determined. A plot of B determined in this way versus 1/C is given in Figure 4.19; the data used for this plot given in Table 4.2. As expected from the previous discussion, the plot is linear with a B-intercept very close to zero. This result not only supports the mechanism for oxygen production discussed above, but shows that the B-term and its connection with the corrosion processes are tied to oxygen production during the early stages of polarization. The calculations also show that a pore-blocking mechanism may explain the interrelationship.

(a) Actually, some of the parameters in this term should vary with current density, particularly V^P and k_1. They may vary, however, in such a way as to be self-negating. For example, V^P and k_1 should both increase with current density, so their quotient may not change appreciably. Nevertheless, further work is warranted to resolve this uncertainty.

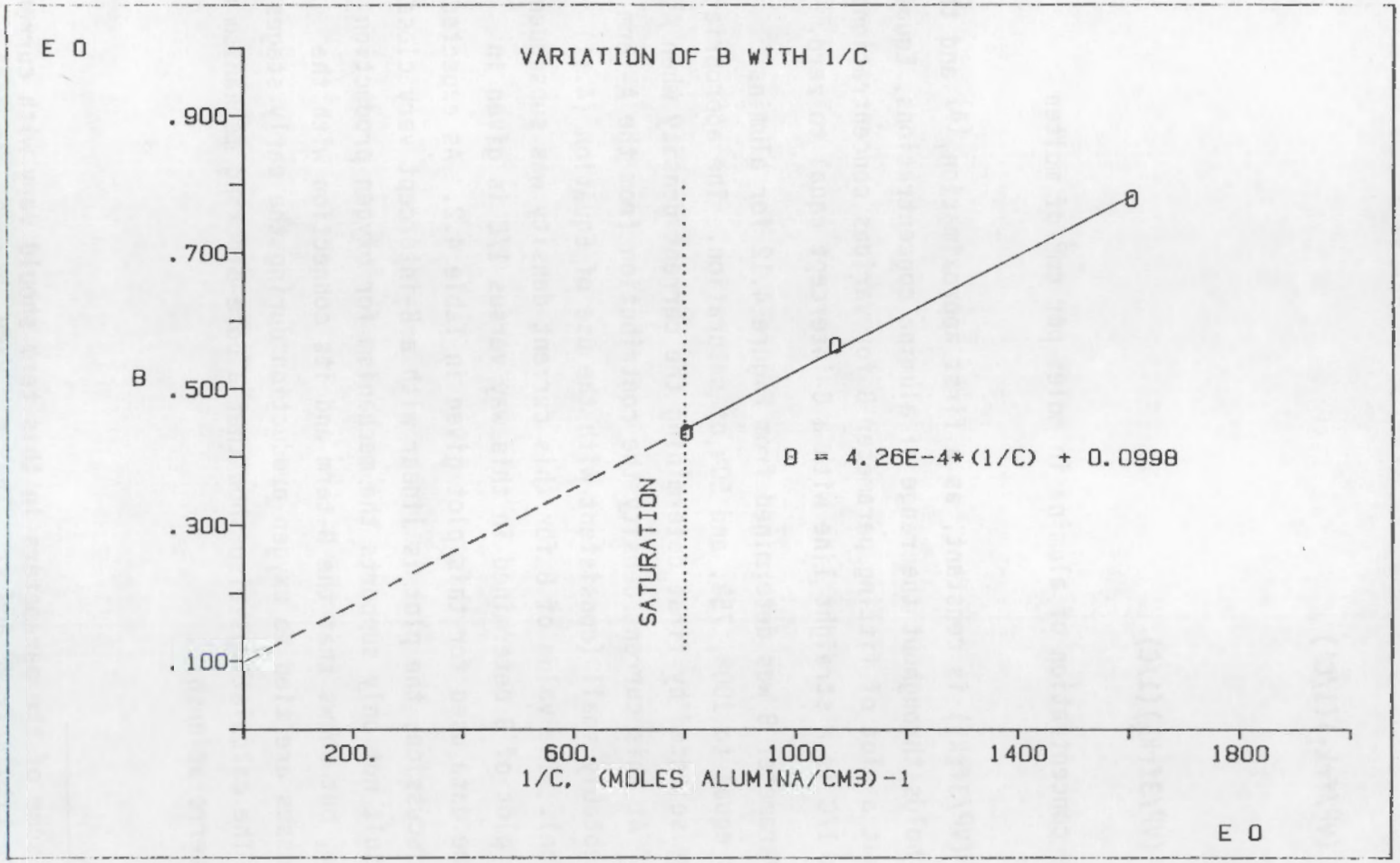

FIGURE 4.19. Variation of Fitting Parameter B with 1/C Where C is the Alumina Concentration in Moles/cm^3.

TABLE 4.2. Data For Plotting Parameter B Against Aluminum Concentration in Moles/cm^3

Al_2O_3 (%) of Saturation	Al_2O_3 (wt%)	C (mole/cm^3)	1/C	B (When A=0)
100	6.0	1.25E-3	802	0.436
75	4.5	9.35E-4	1070	0.564
50	3.0	6.24E-4	1603	0.780

4.5 AN EXPLANATION FOR THE ANODE IMPEDANCE RELATIONSHIP

If a pore-blocking process is responsible for the reduction in the extent of corrosion of the metallic phase of the cermet anodes at higher current densities, then an explanation for the impedance previously associated with a protective film is required.(a) Examination of Figure 4.15c reveals that a certain surface roughening appears to accompany polarization of the anode at higher current densities. The roughness was measured(b) for anodes polarized for identical times using the same conditions except for potential, current density, and alumina concentration. As shown in Figure 4.20, the surface roughness, quantified by parameters x and s, generally decreased as current density increased to about 0.5 A/cm^2. Above 0.5 cm^2, the roughness factors again increased dramatically.

Examination of Figure 4.15b shows that surface roughening accompanies the corrosion reactions at lower current densities. Figure 4.15c shows that the roughening also occurs at higher current densities, although from a presently unexplained source. As mentioned previously, corrosion reactions occurring very shortly after polarization may determine a characteristic morphology on

---

(a) The possibility that a film contributes to the impedance has not been eliminated. Optical microscopy has revealed the presence of a reaction layer, and its analysis is in progress. However, preliminary inspection shows that its characteristics such as thickness, unlike the surface roughness, do not seem to correlate with the measured impedance.

(b) Surface roughness was determined by computing the mean, x, and standard deviation, s, of numerous measurements of the distance between the anode's surface and a reference point using optical micrographs of the anode sample. x gives an indication of the "depth" of the roughness, and s measures the extent of "bumpiness."

the anode's surface. Despite this uncertainty, however, the roughness may help explain the impedance relationships observed in previous PNL studies.

The variation in surface roughness with current density, similar to the relationship involving cell impedance,[(a)] is shown in Figure 4.20. Impedance is highly dependent on cell geometry, including electrode area and topography. It is possible, therefore, that the observed relationship between impedance and current density is caused by changes in surface roughness which, in turn, are determined by the anodic current density.

One possible explanation for the observed correlations is that only a portion of the total surface area is active, i.e. serves as a substrate on which the oxide ions are discharged. On a rough surface, the active regions would probably be those areas which protrude the most into the electrolyte. Recessed areas may be blocked by gas bubbles or, perhaps, solid, poorly conducting corrosion products. In any event, as a result of the roughening, a large portion of the surface area is rendered inactive, causing the "real" surface area to be less than that which is "apparent." The resulting impedance would be larger than expected.

The above explanation for the variation in cell impedance can also help explain certain issues that were puzzling in the context of the alternative film-formation theory. First, the increase in impedance at lower current densities could not be explained because a protective film was not formed appreciably under these conditions. Also, in a number of previous studies at PNL it was observed that the anode impedance could be preserved when the anode was removed from the molten electrolyte and used at a later date in another cell. This observation was explained by proposing that the film which formed on the anode could be preserved during the transfer, i.e. the film formed in the molten electrolyte under polarization conditions could exist intact on the electrode after its removal. This explanation was somewhat suspect since microscopic examination gave no unequivocal evidence for such an intact layer. It was also improbable that the film could retain its chemical integrity

---

(a) This impedance was determined from the high-frequency Z'-intercept of the plots in Figures 4.16 and 4.17. The values, determined in this way, follow the same relationship with current density reported previously (Strachan 1988) and correspond primarily to the electrolyte resistance.

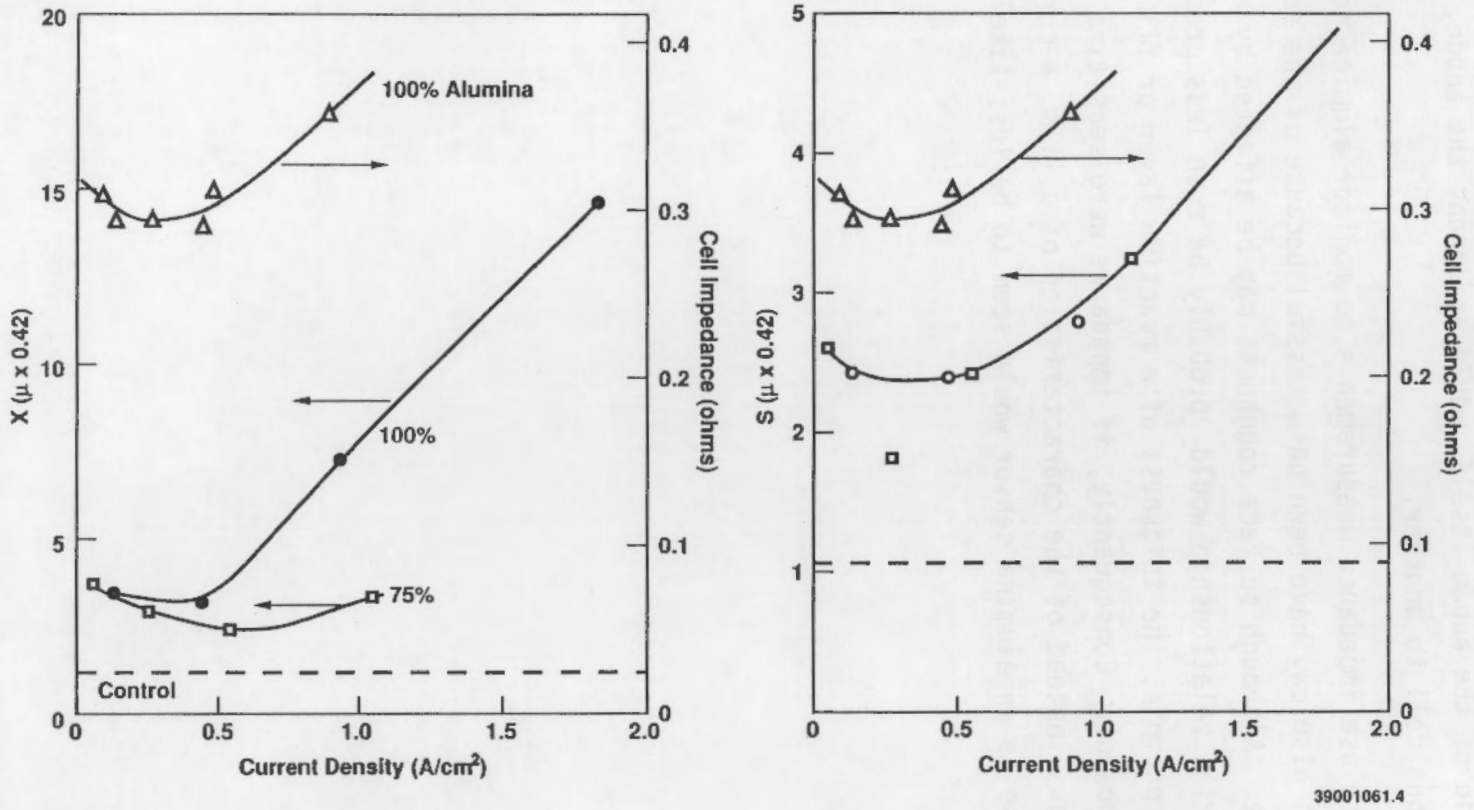

FIGURE 4.20. Relationships of Impedance and Roughness Factors X and S for PNL Cermet Inert Anodes. Data Are For 100% (•, Δ) and 75% (□) Alumina and For an Unpolarized Specimen.

considering the drastic physical and chemical changes accompanying the electrode transfer. It is more likely that the effects of surface roughness, a characteristic of the anode itself, would accompany the anode, surviving a transfer from one cell to another.

Attempts to use impedance measurements to monitor alumina concentration (Windisch 1990) also may have been unsuccessful because of the source of the anode impedance. Although surface roughness may be affected by alumina concentration, the relationship would probably be much less precise than one involving, for example, the thickness of a reaction layer or film (as previously proposed). Consequently, if impedance were sensitive primarily to surface roughness instead of the characteristics of a film, a correlation adequate for use as an alumina sensor would seem to be less likely.

5.0 CONCLUSIONS

The results of potential-step studies, electrochemical impedance spectroscopy, and post-mortem microscopic analysis of polarized anodes suggest that the processes of corrosion of the metallic phase of the cermet anode and the production of oxygen gas are separable and exhibit very different kinetic behavior. The corrosion reactions occur predominantly at low anode potentials, appear to show diffusion control, and may be related to the porosity of the anode. The oxygen production reaction is the predominant reaction above 2.2 V, shows activation control, occurs primarily on the surface of the anode, and is accompanied by an increase in surface roughness at higher current densities. These studies suggest that the production of oxygen shuts down the corrosion reactions, possibly through a pore-blocking mechanism, and contributes to a surface roughening that may help explain some of the impedance relationships previously observed by PNL for the cermet inert anodes. The formation of a protective layer or film is not unequivocally ruled out by the results of these studies. However, alternative mechanisms for the apparent attenuation of corrosion reactions at typical operating current densities should be considered more viable explanations of observed behavior. In particular, the effects of surface porosity and roughness should be more closely examined as indicators (or predictors) of long-term corrosion behavior.

6.0 REFERENCES

Bard, A. J., and L. R. Faulkner. 1980. Electrochemical Methods. John Wiley and Sons, Inc., New York.

Burgman, J. W., J. A. Leistra, and P. J. Sides. 1986. "Aluminum/Cryolite Reference Electrodes for Use in Cryolite-Based Melts." J. Electrochem. Soc. 133(3):496-500.

deLevie, R. 1967. Advances in Electrochemistry and Electrochemical Engineering: Volume 6. Interscience, Wiley, New York.

Macdonald, D. D. Transient Techniques in Electrochemistry. 1977. Plenum Press, New York.

Sato, N., and M. Cohen. 1964. "The Kinetics of Anodic Oxidation of Iron in Neutral Solution." J. Electrochem. Soc. 111(5):512-519.

Sterten, A. 1980. "Structural Entities in NaF-AlF_3 Melts Containing Alumina." Electrochimica Acta. 25:1673-1677.

Strachan, C. M., O. H. Koski, S. C. Marschman, C. H. Schilling and C. F. Windisch. 1988. Fiscal Year 1986 Annual Report for the Inert Electrodes Program. PNL-6746, Pacific Northwest Laboratory, Richland, WA.

Tarcy, G. P. 1986. "Corrosion and Passivation of Cermet Inert Anodes in Cryolite-Type Electrolytes." Light Metals 1986. Warrendale, PA.

Thonstad, J. 1968. "Anodic Overvoltage on Platinum in Cryolite-Alumina Melts." Electrochimica Acta. 13:449-456.

Thonstad, J. 1970. "The Electrode Reaction on the C, CO_2 Electrode in Cryolite-Alumina Melts - II. Impedance Measurements." Electrochimica Acta. 15:1581-1595.

Windisch, Jr., C. F., and N. D. Stice. 1990. Fiscal Year 1989 Annual Report for the Sensors Development Program. PNL-7309. Pacific Northwest Laboratory, Richland, WA.

DISTRIBUTION

No. of Copies

OFFSITE

M. J. McMonigle
U.S. Department of Energy
Office of Industrial Programs
Forrestal Building
Washington, DC 20585

P. H. Salmon-Cox
U.S. Department of Energy
Office of Industrial Programs
Forrestal Building
Washington, DC 20585

12 DOE Office of Scientific and Technical Information

C. Anderson
Columbia Aluminum Co.
85 John Day Dam Road
Goldendale, WA 98620

J. V. Anderson
WCVE3
EG&G Idaho, Inc.
Idaho Falls, ID 83415

D. Auburg
Bonneville Power Administration
P.O. Box 3621, PDX 97208
Portland, OR 97208

F. W. Baker
Ceramics Division
Alcoa Laboratories
Alcoa Center, PA 15069

M. Baltzell
Eastalco Aluminum Company
Alumax, Inc.
5601 Manor Woods
Frederick, MD 21701

No. of Copies

J. A. Barclay
U.S. Bureau of Mines
2401 "E" Street N.W.
Washington, DC 20241

H. Robert Baumgartner
Ceramics Division
Alcoa Laboratories
Alcoa Center, PA 15069

T. R. Beck
Electrochemical Technology Corp.
1601 Dexter Avenue
Seattle, WA 98109

S. Berwagan
Bonneville Power Administration
P.O. Box 3621 K
Portland, OR 97208

T. M. Besmann
Metals and Ceramics Division
Oak Ridge National Laboratory
P.O. Box X, Bldg. 4515
Oak Ridge, TN 37831-6063

K. A. Blakely
President
Advanced Refractory Technologies, Inc.
699 Hertel Ave.
Buffalo, NY 14207

M. H. Blenk
Du Pont
P.O. Box 787
Niagara Falls, NY 14302

No. of
Copies

L. G. Boxall
Martin Marietta Laboratories
1450 South Rolling
Baltimore, MD 21227

J. Bracher
Kaiser Aluminum and Chemical
Corp.
825 N.E. Multnomah St.,
Suite 960
Portland, OR 97232-2150

R. Brandt
Department of Materials Science
and Engineering
University of Washington FB-10
Seattle, WA 98195

J. J. Brown, Jr.
Materials Engineering
Virginia Polytechnic Institute
Blacksburg, VA 24061

A. Budner
Bonneville Power Administration
P.O. Box 3621--EPA
Portland, OR 97208

A. J. Caputo
Metals and Ceramics Division
Oak Ridge National Laboratory
P.O. Box X
Oak Ridge, TN 37831-6063

N. Clark
Bonneville Power Administration-
Industrial Conservation
P.O. Box 3621
Portland, OR 97208

A. Cooke
Martin Marietta Laboratories
1450 South Rolling
Baltimore, MD 21227

No. of
Copies

J. A. Coppola
Standard Oil Engineered
Materials Company
P.O. Box 156
Niagara Falls, NY 14302

D. D. Cudaback
Director
Washington State Dept of Trade
and Economic Development
312 First Avenue North
Seattle, WA 98109

R. Curtis
Materials Development
Corporation
81 Hicks Avenue
Medford, MA 02155

J. V. Day
Kaiser Aluminum and Chemical
Corp
E2111 Hawthorne Road
Mead, WA 99021

R. Dethlefsen
Maxwell Laboratories
8888 Balboa Ave
San Diego, CA 92123

D. H. DeYoung
Alcoa Technical Center
Alcoa Center, PA 15069

S. Diamond
Battelle Columbus Laboratories
505 King Avenue
Columbus, OH 43201-2693

C. W. Doerr
The Stackpole Corporation
Cermag Division
201 Stackpole Street
St. Marys, PA 15847

No. of
Copies

T. Dwonch
Snake River District
BPA
101 W. Poplar
Walla Walla, WA 99362

G. L. Eitel
Stone & Webster Engineering
Corp.
Greenwood Plaza Box 5406
Denver, CO 80217

R. Engdahl
Deposits and Composites, Inc.
318 Victory Drive
Herndon, VA 22070

J. F. Elliott
MIT
Room 4-138
77 Massachusetts Avenue
Cambridge, MA 02139

B. G. Epstein
A. D. Little, Inc.
955 Lenfant Plaza SW 4200
Washington, DC 20024-2119

J. W. Evans
University of California
Dept of Matl. Sci. and Mineral
Eng.
Berkeley, CA 94720

R. A. Fenimore
ICI Advanced Materials
Rollins Building, Eighth Floor
Wilmington, DE 19897

D. A. Figgins
ARCO Petroleum Products Co.
P.O. Box 61004
Anaheim, CA 92803-6104

No. of
Copies

P. Foster
Alcoa Laboratories
P.O. Box 772
New Kinsington, PA 15068

J. Gee
Great Lakes Research Corp
P.O. Box 1031
Elizabethton, TN 37643

T. Gilligan
Eltech Systems Corp.
625 East Street
Fairport Harbor, OH 44077

W. M. Goldberger
Superior Graphite Co.
120 S. Riverside Plaza
Chicago, IL 60606

J. Goodwell
Center for Metals Production
Mellon Institute
4400 Fifth Avenue
Pittsburgh, PA 15213

J.A.S. Green
Martin Marietta Laboratories
1450 South Rolling
Baltimore, MD 21227

C. Griffin
Ceramatec Inc.
2425 S. 900 West
Salt Lake City, UT 84119

L. I. Grindstaff
Great Lakes Research Corp.
P.O. Box 1031
Elizabethon, TN 37643

J. Haggerty
MIT
Building 12, Room 009
77 Massachusetts Avenue
Cambridge, MA 02139

No. of
Copies

I. L. Harry
Electric Power Research
Institute
P.O. Box 10412
Palo Alto, CA 94303

W. E. Haupin
2820 7th Street Road
Lower Burrell, PA 15068

R. Hill
Union Carbide Corp.
P.O. Box 94637
Cleveland, OH 44101

H. F. Hillegass
Alcoa Wenatchee Works
P.O. Box 221
Wenatchee, WA 98807

D. G. Howitt
College of Engineering
University of California, Davis
Davis, CA 95616

F. R. Huettig
Advanced Magnetics, Inc.
45 Corey Lane
Mendham, NJ 07945

G. R. Hyde
U.S. Bureau of Mines
2401 "E" Street N.W.
Washington, DC 20241

S. C. Jacobs
Primary Processing
Aluminum Company of America
Alcoa Technical Center
Alcoa Center, PA 15069

S. H. Jan
Tennessee Valley Authority
1850 Commerce Union Bank Bldg.
Chattanooga, TN 37401

No. of
Copies

N. Jarrett
149 Jefferson Avenue
New Kinsington, PA 15068

J. Johnson
Intalco Aluminum Company
P.O. Box 937
Ferndale, WA 98248

M. H. Johnson
Alcoa Wenatchee Works
P.O. Box 221
Wenatchee, WA 98801

L. Joo
Great Lakes Research Corp
P.O. Box 1031
Elizabethon, TN 37643

M. Karmous
Oregon State Department of
Energy
625 Marion Street, N.E.
Salem, OR 97310

R. Keller
RD 3 Roundtop Road
Export, PA 15632

K. Krupinski
Mail Stop 57
U.S. Steel Technical Center
1 Technical Center Drive
Monroeville, PA 15146

G. Y. Lai
Cabot Corporation
P.O. Box 9013
Kokomo, IN 46902-9013

R. A. Landy
Director of Research
North American Refractories Co.
3127 Research Dr.
State College, PA 16801

No. of
Copies

J. E. Lane
Ceramic Research and
Development Center
Westinghouse Electric
Corporation
1310 Beulah Road
Pittsburgh, PA 15235

Sai-Kwing Lau
Standard Oil Engineered
Materials Company
Niagara Falls R&D Center
P.O. Box 832
Niagara Falls, NY 14302

J. J. Leddy
Dow Chemical U.S.A.
1776 Building
Midland, MI 48640

W. W. Liang
Gas Research Institute
8600 West Bryne Mawr Avenue
Chicago, IL 60631

W. H. Link
Columbia Aluminum Corp.
85 John Day Dam Road
Goldendale, WA 98620

Steve Loftness
Washington State Energy Office
400 E. Union
Olympia, WA 98504

W. Long
Building B815
Dow Chemical
Freeport, Texas 77541

A. G. Longmuir
Kaiser Aluminum and Chemical
Corp.
P.O. Box 877
Pleasonton, CA 94566

No. of
Copies

R. A. Lowden
Metals and Ceramics Division
Oak Ridge National Laboratory
P.O. Box X, Bldg, 4515
Oak Ridge, TN 37831-6063

W. N. Maclay
Koppers Company, Inc.
440 College Park Drive
Monroeville, PA 15146

J. C. McCloskey
Ten Mile River Associates
296 Mt. Hope Street
North Attleboro, MA 02760

S. C. Manaktala
Manager of Technology
Reduction Division
Kaiser Aluminum and Chemical
Corp
300 Lakeside Drive
Oakland, CA 94643

V. H. Markant
Du Pont
P.O. Box 787
Niagara Falls, NY 14302

C. J. McMinn
Extractive Metallurgical
Department
Reynolds Metals Company
P.O. Box 1200
Sheffield, AL 35660

C. H. McMurtry
Standard Oil Engineered
Materials Company
Niagara Falls R&D Center
P.O. Box 832
Niagara Falls, NY 14302

M. A. Mitnick
Avco Specialty Materials
Subsidiary of Textron Inc.
2 Industrial Avenue
Lowell, MA 01851

No. of
Copies

H. Mortensen
R. Palika
Cercom, Inc.
P.O. Box 70
Vista, CA 92083

A. Moussa
A. D. Little, Inc.
20 Acorn Park
Cambridge, MA 02140

B. C. Mutsuddy
Battelle Columbus Division
505 King Avenue
Columbus, OH 43201-2693

P. Ness
Senior Project Manager
Washington State Dept of Trade
and Economic Development
312 First Avenue North
Seattle, WA 98109

A. N. Patel
Battelle Columbus Laboratories
505 King Avenue
Columbus, OH 43201-2693

J. R. Payne
Kaiser Aluminum and Chemical
Corp.
P.O. Box 877
Pleasanton, CA 94566

T. Payne
Columbia Falls Aluminum Co.
Columbia Falls, MT

W. Pebley
Oregon Freeze Dry Corp.
525 25th Avenue SW
P.O. Box 1048
Albany, OR 97321

No. of
Copies

K. Peterson
Columbia Aluminum Corp.
85 John Day Dam Road
Goldendale, WA 98620

R. D. Peterson
Reynolds Metals Company
P.O. Box 1200
Sheffield, AL 35660

T. R. Pritchett
Kaiser Aluminum and Chemical
Corp.
P.O. Box 877

W. W. Pritsky
Aluminum Association
900 19th St. N.W.
Washington, DC 20006

S. P. Ray
Alcoa Technical Center
Alcoa Center, PA 15069

J. F. Rhodes
Advanced Composite Materials
Corp.
1525 S. Buncomb Rd.
Greer, SC 29651

N. E. Richards
Reduction Laboratory
Reynolds Aluminum Corporation
P.O. Box 1200
Sheffield, AL 35660

J. J. Ritter
Ceramics Division
National Bureau of Standards
Gaithersburg, MD 20899

R. C. Rohwedder
3028 Ohio Street
Longview, WA

No. of
Copies

J. Rosling
Myers Metals and Minerals
459 Colman Building
Seattle, WA 98104

D. R. Sadoway
MIT
Room 8-109
77 Massachusetts Avenue
Cambridge, MA 02139

W. Scott
Department of Materials Science
& Engineering
Wilcox Hall FB-10
University of Washington
Seattle, WA 98195

D. R. Secrist
Great Lakes Research Corp.
P.O. Box 1031
Elizabethon, TN 37643

A. B. Shah
Noranda Aluminum, Inc.
P.O. Box 70
New Madras, MO 63869

N. Shelton
Intalco
1300 S. W. 5th, Suite 3508
Portland, OR 97201

F. W. Spillers
Dow Chemical U.S.A.
B-1210 Building
Freeport, TX 77541

Dr. Richard M. Spriggs
Office of the Director
Center for Advanced
Ceramic Technology
Alfred University
Alfred, NY 14802

No. of
Copies

D. V. Stewart
Reynolds Metals Co.
P.O. Box 1200
Sheffield, AL 35660

D. Strahan
Reynolds Metals Company
P.O. Box 27003
Richmond, VA 23261

A. T. Tabereaux
Reynolds Metals Company
P.O. Box 1200
Sheffield, AL 35660

G. P. Tarcy
Aluminum Company of America
Alcoa Technical Center
Alcoa Center, PA 15069

P. Thaure
Primary Planning and Production
Alumax
400 S. El Camino Rd.
San Mateo, CA 94402

W. H. Thielbahr
Conservative Technology
Division
DOE-Idaho Operations Office
785 DOE Place
Idaho Falls, ID 83402

S. Thomson
General Manager
Klickitat PUD
1313 S. Columbus
Goldendale, WA 98620

R. Unger
Merner Research
P.O. Box 248
Ridgewood, NJ 07451

No. of
Copies

A. Vinnard
Bonneville Power Administration
(KWI)
P.O. Box 3621
Portland, OR 97208

T. Von Muller-KWI
Bonneville Power Administration
P.O. Box 3621
Portland, OR 97208

D. H. Weinblatt
AIMCOR
One Parkway North
Deerfield, IL 60015

J. D. Weyand
EG&G Idaho, Inc.
Idaho Falls, ID 83415

B. Wilcox
Northwest Aluminum Co.
3313 W. Second St.
The Dalles, OR 97058

C. B. Wilson
Dow Chemical U.S. A.
Texas Operations
B-101 Building
Freeport, TX 77541

J. C. Withers
Keramont Research Corporation
4233 S. Fremont Avenue
Tucson, AZ 85714

W. A. Zdaniewski
Engelhard Corporation
Menlo Park, CN 28
Edison, NJ 08818

FOREIGN

D. Brodie
Comalco Ltd.
55 Collins St.
Melbourne, AUSTRALIA

No. of
Copies

H. Connor
Group Licensing Controller
Johnson Matthey, plc
New Garden House
78 Hatton Garden
London EC1N 8JP ENGLAND

L. Dion
Alcan International Limited
C.P. 6090
Montreal, Quebec
CANADA, H3C 3H2

T. Kjar
Comalco Ltd.
55 Collins St.
Melbourne, AUSTRALIA

E. W. Dewing
Alcan International
P.O. Box 8400
Kingston, Ontario
CANADA K7L 4Z4

D. N. MacMillan
Alcan International
C.P. 1250
Jonquieve, Quebec
CANADA G7S 4K8

J. H. Reimers
Jan H. Reimers and Associates
Inc.
221 Lakeshore Road East
Oakville, Ontario
CANADA, L6J 1H7

A. Oye
Institute of Inorganic Chemistry
Norwegian Institute of Technology
University of Trondheim
N-7034 Trondheim-NTH, NORWAY

No. of
Copies

J. Thonstad
Laboratories of Industrial
Electrochemistry
Norwegian Institute of
Technology
University of Trondheim
N-7034 Trondheim-NTH, NORWAY

K. O. Vee
ASV Ardal Verk
N-5875 Ardalstargen, NORWAY

ONSITE

DOE - Richland Operations Office

R. B. Goranson

No. of
Copies

25 Pacific Northwest Laboratory

M. Clement
N. C. Davis
D. K. Hilliard
G. L. McVay
N. L. Moore
L. G. Morgan (10)
C. H. Schilling
D. M. Strachan
R. E. Westerman
C. F. Windisch
Publishing Coordination
Technical Report Files (5)